

Evaluation of Eight Current Reanalyses in Simulating Land Surface Temperature from 1979 to 2003 in China

CHUNLÜE ZHOU, KAICUN WANG, AND QIAN MA

College of Global Change and Earth System Science, Beijing Normal University, Beijing, China

(Manuscript received 22 December 2016, in final form 5 June 2017)

ABSTRACT

Land surface temperature T_s provides essential supplementary information to surface air temperature, the most widely used metric in global warming studies. A lack of reliable observational T_s data makes assessing model simulations difficult. Here, the authors first examined the simulated T_s of eight current reanalyses based on homogenized T_s data collected at ~ 2200 weather stations from 1979 to 2003 in China. The results show that the reanalyses are skillful in simulating the interannual variance of T_s in China ($r = 0.95$) except over the Tibetan Plateau. ERA-Interim and MERRA land versions perform better in this respect than ERA-Interim and MERRA. Observations show that the interannual variance of T_s over the north China plain and south China is mostly influenced by surface incident solar radiation R_s , followed by precipitation frequency, whereas the opposite is true over the northwest China, northeast China, and the Tibetan Plateau. This variable relationship is well captured by ERA-Interim, ERA-Interim land, MERRA, and JRA-55. The homogenized T_s data show a warming of $0.34^\circ\text{C decade}^{-1}$ from 1979 to 2003 in China, varying between 0.25° and $0.42^\circ\text{C decade}^{-1}$ for the eight reanalyses. However, the reanalyses substantially underestimate the warming trend of T_s over northwest China, northeast China, and the Tibetan Plateau and significantly overestimate the warming trend of T_s over the north China plain and south China owing to their biases in simulating the R_s and precipitation frequency trends. This study provides a diagnostic method for examining the capability of current atmospheric/land reanalysis data in regional climate change studies.


1. Introduction


Near-surface air temperature T_a provides key evidence for global warming and has been widely used to study global climate change. The observed global warming has been mainly attributed to anthropogenic greenhouse gases. Gradually, scientists and the public become more interested in climate change in the region in which they live. The mechanism underlying regional climate change is more complicated because it is determined by greenhouse gases and multiple feedbacks (Zhou and Wang 2016a,d). Among them, the effect of land surface energy feedback on regional climate change

has been studied less frequently and is a more challenging topic.

Land surface radiation budget is even a stronger determining factor of the evolution of land surface temperature T_s . After the sun rises, the surface is heated by surface-absorbed solar radiation. To balance the surface-absorbed radiation, the surface emits longwave radiation, which is determined by T_s . The surface net radiation is partitioned into latent and sensible heat fluxes, and the latter directly warms the air over the surface (Zhou and Wang 2016c). Surface vegetation coverage and its wetness play an important role in the partitioning of the surface net radiation and therefore changes of T_a and T_s at regional scales.

Nowadays, the current reanalysis products have been widely used in climate studies as important auxiliary observations (Thorne and Vose 2010; Dee et al. 2011a). In reanalyses, the energy budget is closely

 Denotes content that is immediately available upon publication as open access.

 Supplemental information related to this paper is available at the Journals Online website: <http://dx.doi.org/10.1175/JCLI-D-16-0903.s1>.

Corresponding author: Kaicun Wang, kcwang@bnu.edu.cn



This article is licensed under a Creative Commons Attribution 4.0 license (<http://creativecommons.org/licenses/by/4.0/>).

associated with T_s (Viterbo and Beljaars 1995; Trigo et al. 2015). Although the importance of T_s has been recognized, the accuracy of reanalyzed T_s products over land is not well understood, mainly because of the lack of global station-based T_s observations.

The examination of simulated T_s from reanalyzed models can provide insight into the parameterization of land surface processes (Wang et al. 2014; Trigo et al. 2015). Using limited station- and satellite-based T_s observations, several existing studies have revealed that surface incident solar radiation R_s dominates the change in T_s and that surface–atmosphere conditions, including land cover, soil moisture, soil texture, and the temperature–moisture profile, substantially influence T_s (Wen et al. 2003; Weng et al. 2004; Xiao and Weng 2007; Good 2016; Guo et al. 2016).

A few studies have revealed an underestimation of the diurnal variance in the modeled T_s over sparsely vegetated regions (Zeng and Dickinson 1998; Yang et al. 2002; Chen et al. 2010, 2011; Zheng et al. 2012; Wang et al. 2014; Trigo et al. 2015). Much effort has been put forth to develop T_s parameterizations for land surface models. Yang et al. (2002) reparameterized surface roughness (controlling the latent and sensible heat fluxes) to improve the available energy partitioning and to further meliorate the diurnal variance of the modeled T_s over the Tibetan Plateau and dry land of China (Chen et al. 2010, 2011). Zeng et al. (2012) improved the modeled T_s over bare soil surfaces by modifying the surface roughness and constraining the minimum friction velocity. Apart from these revisions in land surface model parameterizations, Wang et al. (2014) indicated that atmospheric forcing data and assimilation systems have an important impact on the modeling of T_s .

Zheng et al. (2012) found that the NCEP operational Global Forecast System (GFS) has a large cold bias in daytime T_s over the western United States and adopted new vegetation-dependent formulations of the momentum and thermal roughness lengths to reduce this bias. Trigo et al. (2015) found a slight cold bias in daytime T_s and a warm bias in nighttime T_s for the ECMWF model. Surface roughness (controlling the latent and sensible heat fluxes) and surface conductivity (controlling the ground heat flux) were revised to substantially improve the modeled T_s , although the introduction of realistic vegetation into the model caused a limited improvement in the simulated T_s (Trigo et al. 2015).

Prior evaluations and improvements have mainly been based on comparison of the absolute value of the modeled T_s using only a few T_s observations at a limited number of stations. Because T_s is not routinely measured at meteorological stations under the guidance of the World Meteorological Organization (WMO), T_s

observations are only available for a relatively brief period at a few stations, for example, from the National Oceanic and Atmospheric Administration's Surface Radiation Budget Network (NOAA SURFRAD) (Augustine et al. 2000), FLUXNET (Baldocchi et al. 2001), and the GEWEX Asian Monsoon Experiment (GAME/Tibet) (Ma et al. 2006). In China, however, T_s has been routinely measured since the 1950s, and there are enough available T_s data since the 1960s at approximately 2200 stations. This makes it possible to perform a comprehensive assessment of the modeled T_s in reanalyses, including the climatology, interannual variance, long-term trend, and their controlling factors.

Reanalyses consist of an assimilation system, forecast model, and observation data; thus, the error in reanalyzed outputs is mainly derived from these three components. The above attempt to revise the parameterizations of the surface roughness, surface conductivity, and friction velocity has improved the simulation of the absolute value of T_s , although it remains uncertain whether reanalyses can reproduce the long-term trend (Thorne and Vose 2010; Dee et al. 2011a). Thus, the extent to which reanalyses can represent the observed trend in T_s and the factors affecting the simulated bias in the T_s trend need to be investigated. This examination of the simulated T_s trend is closely related to Earth's surface energy budget and hence to the simulated capacity of climate change by reanalyses.

A previous work (Zhou and Wang 2016b) has utilized satellite-derived T_s to reveal an underestimation of the T_s trend from 2002 to 2015 over approximately 70% of the global desert in the current reanalyses and examined the relationships between interannual variations of T_s and atmospheric circulation changes. However, satellite-retrieved T_s data, based on infrared observations, are only available under clear sky conditions and are of short duration.

Using longer datasets that include T_s , R_s , and precipitation data from 1979 to 2003 at approximately 2200 stations over China, this study further provides a quantitative examination of the reanalyzed T_s , including the climatology, interannual variances, long-term trends, and their controlling factors, from eight reanalysis products. This study quantifies the T_s errors and their dominant factors in reanalysis products, hence providing a better understanding of the modeled T_s error sources and indicating possible improvements for simulating climate change.

2. Data and methods

a. Observation datasets

The latest comprehensive daily dataset, including land surface temperature T_s , precipitation P , 2-m air

temperature T , sunshine duration, relative humidity, and surface pressure from approximately 2400 meteorological stations in China from 1961 to 2014, was obtained from the China Meteorological Administration (CMA; <http://data.cma.cn/data>). This dataset has been subjected to the initial quality control by the CMA, which includes the identification of outliers, an internal consistency check, spatial and temporal consistency checks, artificial checks, and correction of suspected and erroneous data.

To reduce the effects associated with sampling and record length, the stations were required to have at least 95% of the record duration at all time scales (i.e., ≥ 28 days per month, ≥ 347 days per year, and ≥ 24 years during the study period of 1979–2003). As a result, approximately 2200 stations met the requirements and were used in this study (supplemental Fig. S1).

Sunshine duration has been suggested to be the best variable for reconstructing the long-term surface incident solar radiation R_s based on the revised Ångström–Prescott Eq. (1) (Yang et al. 2006; Wang 2014; Wang et al. 2015):

$$R_s/R_c = a_0 + a_1(n/N) + a_2(n/N)^2, \quad (1)$$

where n is the measured sunshine duration, N is the theoretical value of sunshine duration, and R_c is the daily total solar radiation at the surface under clear sky conditions. Here, the sunshine duration represents the period when the direct solar beam irradiance exceeds 120 W m^{-2} . The effects of Rayleigh scattering, water vapor absorption, and ozone absorption can be considered in R_c using previously discussed meteorological observations (Yang et al. 2006; Wang et al. 2015).

Several intensive studies have reported that R_s derived via sunshine duration can accurately depict the interannual, decadal, and long-term variances of R_s (Wang et al. 2012; Wang 2014; Wang et al. 2015). In

addition, this R_s derivation has been shown to accurately reflect the impact of aerosols and clouds on R_s over China (Tang et al. 2011; Wang et al. 2012). The derived R_s is nearly free from the sensitivity drift problem that commonly plagues R_s observations over China (Wang 2014). More details on the derived R_s can be found in Yang et al. (2006) and Wang et al. (2015). In this study, a precipitation event is defined as one day with precipitation of at least 0.1 mm.

b. Reanalysis datasets

In the present study, we used the T_s observations to examine the simulation of T_s in eight current reanalyses, namely, ERA-Interim (Dee et al. 2011b), ERA-Interim land (Balsamo et al. 2015), ERA-20C (Poli et al. 2016), MERRA (Rienecker et al. 2011), MERRA land (Reichle et al. 2011), NCEP-R1 (Kalnay et al. 1996), NCEP-R2 (Kanamitsu et al. 2002), and JRA-55 (Kobayashi et al. 2015). More information on the horizontal and temporal resolution of the eight reanalyses is shown in Table 1.

Reanalyses consist of assimilation system, forecast model, and observation data. MERRA, NCEP-R1, and NCEP-R2 adopt three-dimensional variational data assimilation systems (3D-VAR), whereas ERA-Interim, ERA-Interim land, ERA-20C, JRA-55, and MERRA land employ four-dimensional variational data systems (4D-VAR). ERA-20C only assimilates surface pressure and marine winds (Poli et al. 2016), and the other reanalyses assimilate many of the basic upper-air atmospheric fields, including air temperature, surface pressure, marine winds, radiosonde moisture, satellite radiances, and so on, from multiple sources.

The reanalyzed T_s values are pure model calculations without assimilating T_s observations owing to the lack of a global T_s observing network (Zhou and Wang 2016c). In a reanalysis land surface model, a skin layer without heat capacity is assumed to isolate radiative heating from underlying soil (Viterbo and Beljaars 1995); thus, T_s corresponds to the temperature at the

TABLE 1. Summative information on the reanalyses used in this study. To ensure a consistent length of analysis for all products and observations, the period of 1979–2003 was selected for all reanalyses except MERRA land, for which the period of 1982–2003 was used because the forcing data were spurious in 1980 and 1981.

Reanalysis	Institution	Model resolution	Data resolution	Period	Assimilation system
NCEP-R1	NCEP–NCAR	T62 (~210 km)	$5/2^\circ \times 5/2^\circ$	1948 and afterward	3D-VAR
NCEP-R2	NCEP–DOE	T62 (~210 km)	$5/2^\circ \times 5/2^\circ$	1948 and afterward	3D-VAR
MERRA	NASA GMAO	$1/2^\circ \times 2/3^\circ$ (~55 km)	$1/2^\circ \times 2/3^\circ$	1979 and afterward	3D-VAR
MERRA land	NASA GMAO	$1/2^\circ \times 2/3^\circ$ (~55 km)	$1/2^\circ \times 2/3^\circ$	1980 and afterward	4D-VAR
ERA-Interim	ECMWF	T255 (~80 km)	$3/4^\circ \times 3/4^\circ$	1979 and afterward	4D-VAR
ERA-Interim land	ECMWF	T255 (~80 km)	$3/4^\circ \times 3/4^\circ$	1979 and afterward	4D-VAR
ERA-20C	ECMWF	T159 (~126 km)	$3/4^\circ \times 3/4^\circ$	1900–2010	4D-VAR
JRA-55	JMA	T319 (~55 km)	$5/4^\circ \times 5/4^\circ$	1958–2013	4D-VAR

interface. The reanalyzed T_s data are physically derived from the surface–atmosphere energy balance for each tile during the forecast step of the land surface model [Eq. (2)] (Viterbo and Beljaars 1995; Viterbo et al. 1999), which links the surface with the lowest model level through dry static energy and moisture (Best et al. 2004) and thermal contact with a single four-layer soil profile (or one layer if snow is present) (Dee et al. 2011b). The surface–atmosphere energy balance equation can be written as

$$(1 - f_{R_s})(1 - \alpha)R_s + \varepsilon(R_L - \sigma T_s^4) + H + \text{LE} = C_{\text{surf}}(T_s - T_0) \quad (2)$$

where f_{R_s} is a small fraction of R_s transmitted directly to surface soil, snow, or ice, α is the surface albedo, ε is the longwave emissivity, σ is the Stefan–Boltzmann constant, R_L is the downward longwave radiation, and H and LE are the sensible and latent heat fluxes, respectively. The right-hand side of the equation represents the ground heat flux through coupling with the underlying soil, snow, or ice with temperature T_0 . Moreover, C_{surf} is the surface thermal conductivity, and T_s is the land surface temperature. The area-weighted T_s of each tile is then averaged from the T_s of subtiles; hence, T_s is a prognostic variable of the land surface model.

Different reanalyses have specific schemes that might influence the simulation of T_s , R_s , and precipitation. NCEP-R2 adopts a simple rainfall assimilation over land for improving soil wetness to prevent long-term climate drift of soil wetness (Kanamitsu et al. 2002). The MERRA land (ERA-Interim land) T_s is averaged from an offline land surface model simulation forced by bias-corrected MERRA (ERA-Interim) reanalysis (primarily for precipitation), which is considered more accurate for land surface hydrological studies (Balsamo et al. 2009; Reichle et al. 2011). Precipitation bias corrections preserve water balance closure and are vital for improving land model output (Reichle et al. 2011; Balsamo et al. 2015).

The assimilation of radiosonde temperature–moisture profiles and satellite radiances facilitates the acquisition of cloud parameters and the computation of R_s and precipitation processes (Dee et al. 2011b; Wang et al. 2015; Dolinar et al. 2016). However, the reanalyses do not allow aerosol loadings to change annually, albeit an inclusion of their monthly climatologies (Wang et al. 2015).

c. Method to homogenize the observed time series

Since approximately 2003, the observation infrastructure has been changed from manual to automatic T_s

measurements. Owing to the absence of snow removal for automatic observations, a higher temperature might be obtained from automatic observations. Other problems related to the observation infrastructure (e.g., instrument aging and changes in observing practices) and station relocations can also lead to false time heterogeneity in time series. Therefore, the study period is selected from 1979 to 2003.

To diminish the impact of data homogenization on the trends in the observed T_s , R_s , and precipitation frequency, we used the RHtestsV4 software package (Wang and Feng 2013) to detect and homogenize the breakpoints in the monthly time series. The package involves two algorithms: the PMTred algorithm is based on the penalized maximal t test (PMT) with a reference series (Wang et al. 2007), and the PMFred algorithm is based on the penalized maximal F test (PMF) without a reference series (Wang 2008a). The PMFred algorithm can detect undocumented mean shifts in a time series with a linear trend using a common-trend two-phase regression model (Wang 2008a). If the breakpoint is statistically significant, the quantile-matching (QM) adjustment in RHtestsV4 is recommended for making adjustments to the time series (Wang et al. 2010; Wang and Feng 2013). The QM adjustment aims to match the empirical distributions from all detrended segments with the specific base segment (Wang et al. 2010). Moreover, the QM adjustment also considers a seasonality of discontinuity, the annual cycle, first-order autoregressive errors, and the linear trend in the time series (Wang 2008b; Wang et al. 2010; Wang and Feng 2013). Recently, the PMTred algorithm with the QM adjustment was successfully used to homogenize climatic time series (Dai et al. 2011; Tsidu 2012; Aarnes et al. 2015; Siswanto et al. 2016; Wang and Wang 2016).

We adopted the PMFred algorithm to detect breakpoints at each station. As such, 714 out of 2223 (30.2%) stations have significant breakpoints at a confidence level of 95% for the T_s time series and 804 out of 2223 (36.2%) stations for R_s (Fig. S1). Moreover, 1268 (57%) stations have significant breakpoints for the T_s or R_s time series; an additional 955 (43.0%) stations have original homogenized data (Fig. S1). Considering the change in the observing instrumentation around 2003, we selected the longest available segment from 1979 to 2003 as the base segment and used the QM adjustment to adjust the significant breakpoint at a confidence level of 95%. Moreover, we preliminarily inspected the detected breakpoints with limited station information.

d. Trend calculation and partial linear regression

We interpolated the reanalyzed datasets from different spatial resolutions (Table 1) onto the observed sites

using bilinear interpolation (i.e., a linear interpolation function on two-dimensional grids). When calculating the regional values, we averaged the station data inside $1^\circ \times 1^\circ$ grids using an area-weighted average method to minimize the impact of the heterogeneous distribution of the sites.

To assess the performance of the reanalyzed T_s , the bias, root-mean-square error (RMSE), standard deviation (STD), and correlation coefficient r were used. Furthermore, we compared the trend in the reanalyzed T_s with the observed trend:

$$y = at + b + \varepsilon, \quad (3)$$

where y is the reanalyzed or observed T_s , R_s , and precipitation frequency anomaly relative to the reference period of 1981 to 2000, a is the corresponding trend, t is the year, b is the intercept when $t = 0$, and ε is the equation error. This equation is treated using the ordinary least squares method and the two-tailed Student's t test.

Pearson correlation analysis is often used to reveal the relationship between two variables. However, several of the environmental variables may be linearly covariant with one another (e.g., 48% of the variance in R_s might be accounted for by precipitation frequency over China). The partial least squares approach is a widely applied statistical tool to isolate the relationship between two variables from the confounding effects of several correlated variables (Wold et al. 1984; Radok and Brown 1993; Beer et al. 2010; Carvalhais et al. 2014). In evaluating the relationship between T_s and R_s or precipitation frequency, we used partial least squares to statistically exclude the confounding effects of the other variable:

$$\rho_{(x,y)|z} = \frac{r_{x,y} - r_{x,z}r_{y,z}}{\sqrt{(1-r_{x,z}^2)(1-r_{y,z}^2)}}, \quad \text{and} \quad (4)$$

$$\text{slope}_{(x,y)|z} = \frac{\sigma_y}{\sigma_x} \frac{r_{x,y} - r_{y,z}r_{x,z}}{1-r_{x,z}^2}, \quad (5)$$

where $\rho_{(x,y)|z}$ and $\text{slope}_{(x,y)|z}$ are the partial correlation coefficient and partial regression coefficient, respectively, between the detrended T_s and R_s or precipitation frequency after controlling for the detrended precipitation frequency or R_s ; $r_{x,y}$, $r_{x,z}$, and $r_{y,z}$ are the correlations between the detrended T_s and R_s , T_s and precipitation frequency, and R_s and precipitation frequency, respectively; and σ_y and σ_x are the standard deviations of the detrended T_s and R_s or precipitation frequency. The use of the detrended time series in the above Pearson and partial linear correlation and regression analysis instead of the original nonstationary time series provides a robust estimate of their relationship

(Veizer et al. 2000; Zhou et al. 2007; Podobnik and Stanley 2008).

To evaluate the potential collinearity of the independent variables in the models, we calculated the variance inflation factor (VIF). The VIF for R_s and precipitation frequency were less than 4; that is, VIF of 1.90, 3.09, 1.40, 1.48, 3.12, and 2.34 are obtained over China, northwest China, the Tibetan Plateau, northeast China, the north China plain, and south China, respectively, much less than the threshold of 10, above which the collinearity of models is bound to adversely affect the regression results (Ryan 2008).

3. Results

a. Climatology and bias in land surface temperature

Figure 1 illustrates the bias in T_s from the raw observations and the eight reanalyses relative to the homogenized observations over China. The eight reanalyses roughly underestimate the absolute value of T_s except for ERA-Interim land and ERA-20C over the heart of the north China plain (Fig. 1). The underestimation of T_s in the reanalyses is largest over the Tibetan Plateau (-10.89° to -5.44°C), followed by northwest China (-5.84° to -1.84°C) and south China (-4.21° to -2.81°C), and ending with the north China plain (-3.45° to -1.43°C) and northeast China (-2.97° to -1.36°C) (Fig. 1 and Table 2). The raw T_s observations must be adjusted at more than 30% (714/2223) of the stations, especially over central China (Fig. 1). However, a small adjustment of 0.21°C from the raw T_s observations over 30% of the stations is insufficient for canceling the underestimation of T_s by the reanalyses (Fig. 1). Overall, the eight reanalyses have different simulation capacities for the absolute values of T_s (Fig. 1 and Table 2). ERA-Interim land has the best simulation capacity for the absolute value of T_s , while ERA-20C, NCEP-R1, and NCEP-R2 are the worst in this regard.

The reanalyses rationally reproduce the seasonal cycle of T_s , although they have a larger underestimation in summer than in winter (Fig. 2), which is consistent with the evaluated results of reanalyzed T_s using observations from the U.S. Climate Reference Network (USCRN) stations and MODIS T_s products (Zhou and Wang 2016b). This underestimation likely results from a combination of vegetation growth and an increase in R_s in summer with the addition of a larger overestimated precipitation frequency in summer (than in winter) in the reanalyses (Zhou and Wang 2017).

The underestimated T_s might directly influence the simulation of surface air temperature. Ma et al. (2008)

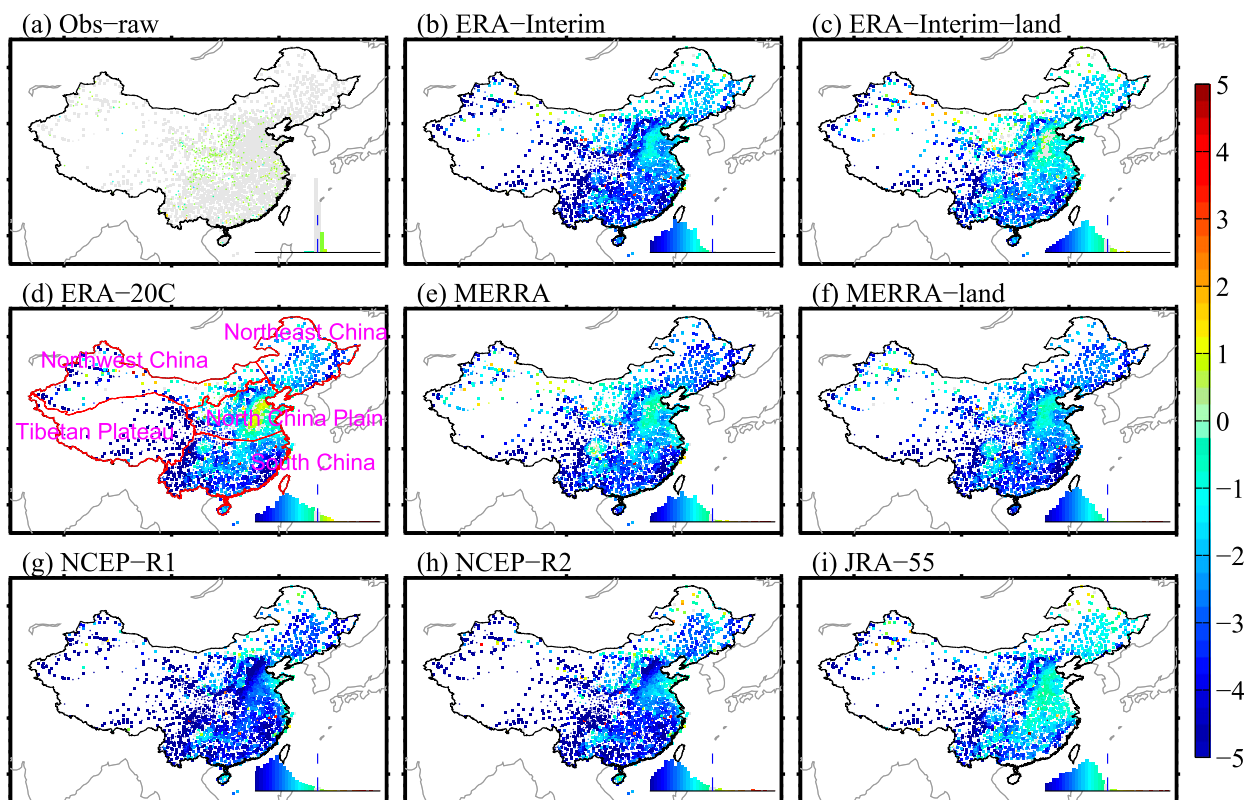


FIG. 1. Bias in land surface temperature T_s ($^{\circ}\text{C}$) from 1979 to 2003 based on the eight reanalysis products: (a) raw observations, (b) ERA-Interim, (c) ERA-Interim land, (d) ERA-20C, (e) MERRA, (f) MERRA-land, (g) JRA-55, (h) NCEP-R1, and (i) NCEP-R2 relative to homogenous observations. The square plot is from the original homogenous time series; the dot plot is from the QM-adjusted homogenous time series [e.g., the green dots in (a) are from the QM-adjusted time series]. Based on topography and the Qinling Mountain–Huaihe River line, China is divided into five subregions, namely, northwest China, the Tibetan Plateau, northeast China, the north China plain, and south China.

reported that ERA-40, NCEP-R1, and NCEP-R2 underestimated surface air temperature in China with a maximum cooling bias in most of western China and suggested that NCEP-R1 had the worst performance. Our simulation results for T_s are very similar to their results and provide a plausible explanation for the underestimated surface air temperature in the reanalyses. Several previous

studies have presented a very small bias in T_a in ERA-Interim (Decker et al. 2012; Wang and Zeng 2012; Zhou and Wang 2016c), which is consistent with the result for T_s . Wang and Zeng (2015) illustrated a larger simulated underestimation of T_a in summer than in winter from simulations using ERA-Interim, MERRA, and NCEP-R1, which is reflected by the T_s simulation in nature (Fig. 2).

TABLE 2. Bias ($^{\circ}\text{C}$) in land surface temperature T_s from 1979 to 2003 over China and its five subregions from ERA-Interim, ERA-Interim land, ERA-20C, MERRA, MERRA land, NCEP-R1, NCEP-R2, JRA-55, and raw observations relative to homogenous observations. The time span of MERRA land starts in 1982 because of false input forcings in 1980 and 1981.

	China	Northwest China	Tibetan Plateau	Northeast China	North China plain	South China
ERA-Interim	-3.72	-3.29	-7.78	-2.03	-2.70	-3.79
ERA-Interim land	-2.50	-1.88	-5.44	-1.36	-1.43	-2.81
ERA-20C	-3.89	-3.02	-10.89	-2.43	-1.51	-3.55
MERRA	-3.29	-1.84	-7.26	-2.97	-2.06	-3.30
MERRA land	-3.46	-2.47	-6.90	-2.82	-2.32	-3.46
NCEP-R1	-4.81	-5.84	-10.03	-2.79	-3.45	-4.21
NCEP-R2	-4.42	-5.82	-8.93	-2.12	-2.75	-4.19
JRA-55	-3.31	-3.78	-7.38	-1.41	-2.25	-2.76
Obs-raw	0.05	0.03	0.01	0.03	0.09	0.06

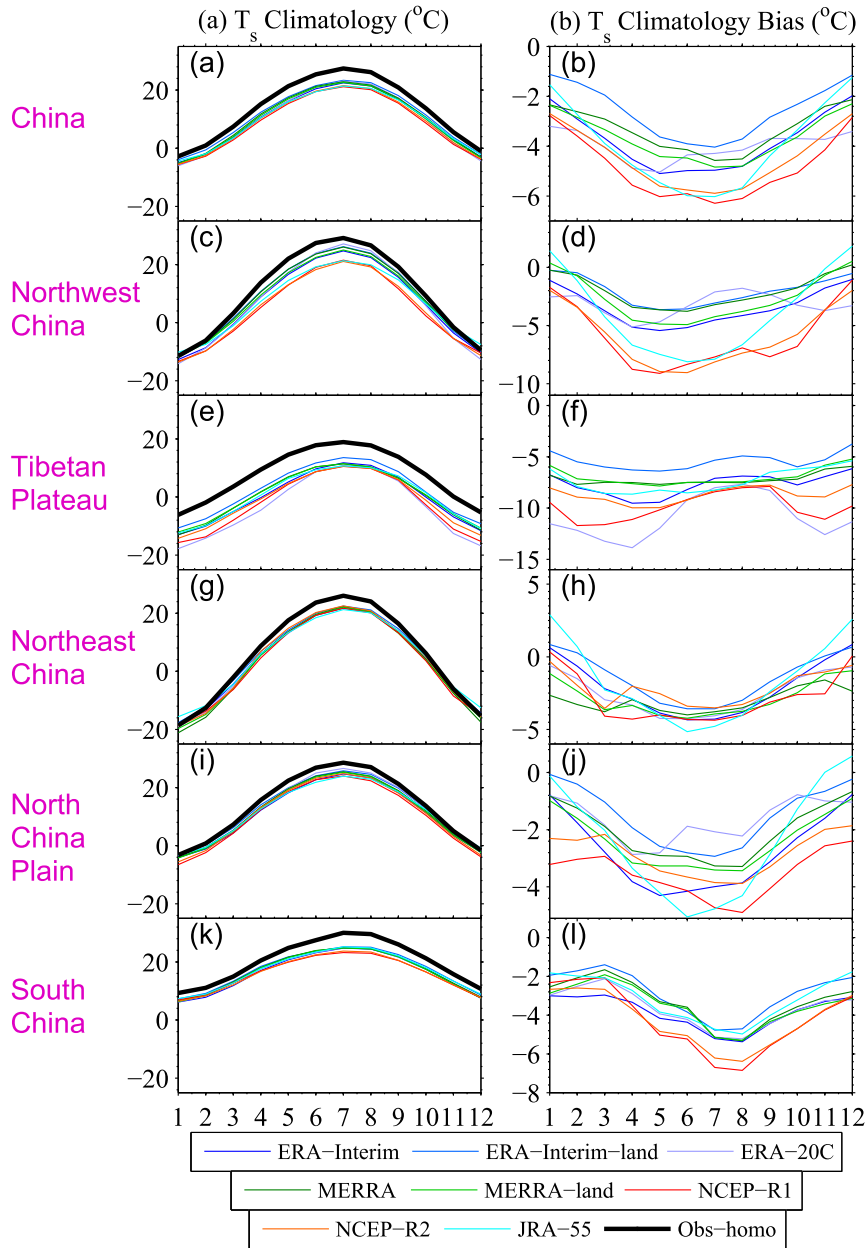


FIG. 2. (left) The 1981 to 2000 climatology and (right) the bias land surface temperature T_s from the eight reanalysis products from 1979 to 2003 over China, northwest China, the Tibetan Plateau, northeast China, the north China plain, and south China relative to the homogeneous T_s observation.

b. Interannual variability of land surface temperature

In this study, we paid more attention to the interannual variability and trend of T_s than to its climatology. Figure 3 shows Taylor diagrams of the observed and reanalyzed annual T_s anomalies over China and its five subregions. We found that the correlations between these reanalyzed and observed annual T_s anomalies are

relatively strong (Fig. 3). Among them, NCEP-R1 and NCEP-R2 have relatively weak correlations (0.1 and 0.4, respectively) over the Tibetan Plateau.

ERA-Interim, JRA-55, ERA-Interim land, MERRA, and MERRA land perform well in terms of the simulated T_s anomaly over China ($r = 0.95$; $RMSE = 0.1^\circ\text{C}$) (Fig. 3a) and its subregions ($r = 0.9$; $RMSE = 0.2^\circ\text{C}$) (Figs. 3b–f). ERA-20C always presents a large standard

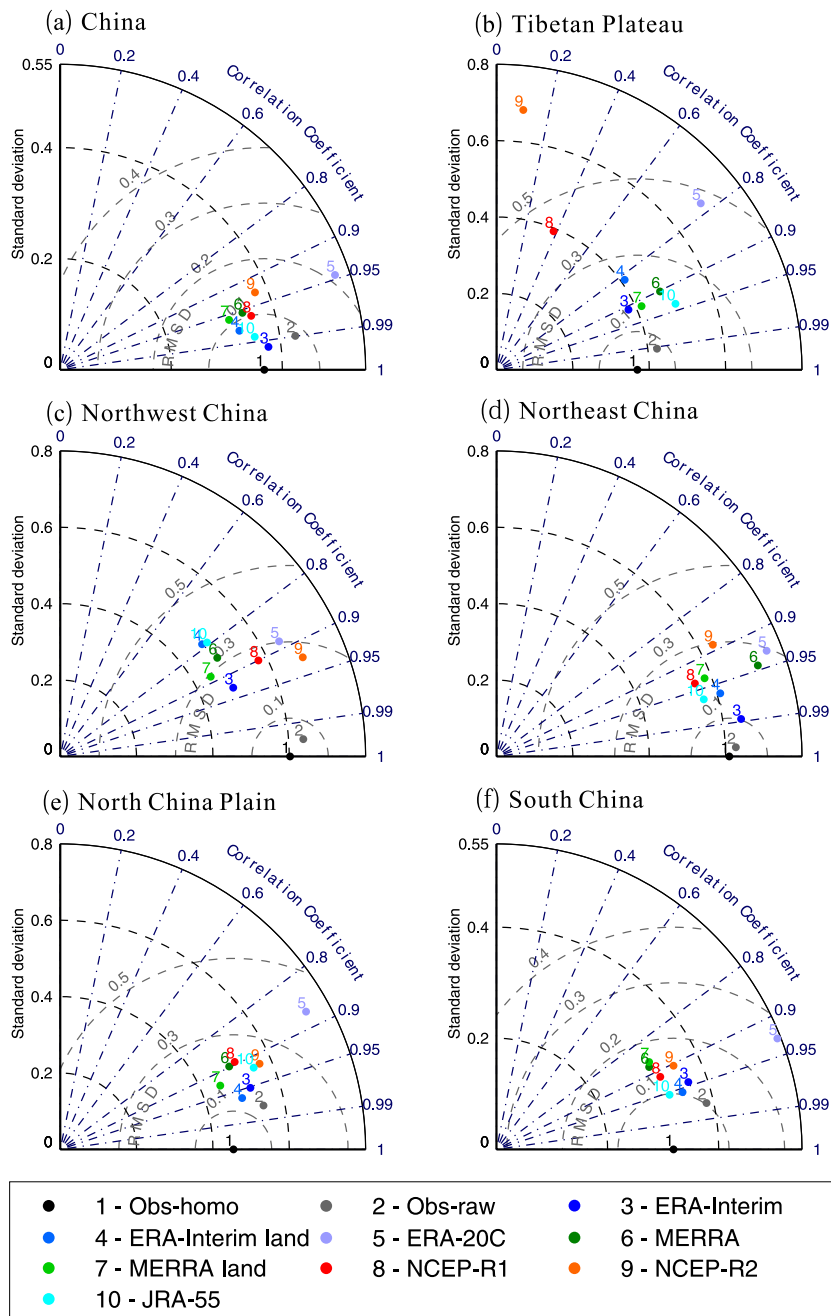


FIG. 3. Taylor diagrams for the annual time series of the observed and reanalyzed land surface temperature anomalies T_s from 1979 to 2003 in China. The correlation coefficient, standard deviation, and RMSE are calculated against the observed T_s anomaly.

deviation in T_s and hence a large RMSE over China and its subregions (Fig. 3), which likely results from less assimilation of multiple observations and incomplete parameterization schemes (Poli et al. 2016).

Compared with the T_s from ERA-Interim and MERRA, the T_s from the land surface products (i.e., ERA-Interim land and MERRA land) have a smaller

standard deviation and RMSE (Fig. 3), maybe because the offline land surface models merge the observed precipitation dataset and hence improve the partitioning of available energy over land (Reichle et al. 2011; Balsamo et al. 2015). In addition, T_s over south China is depicted most accurately by the reanalyses (Fig. 3).

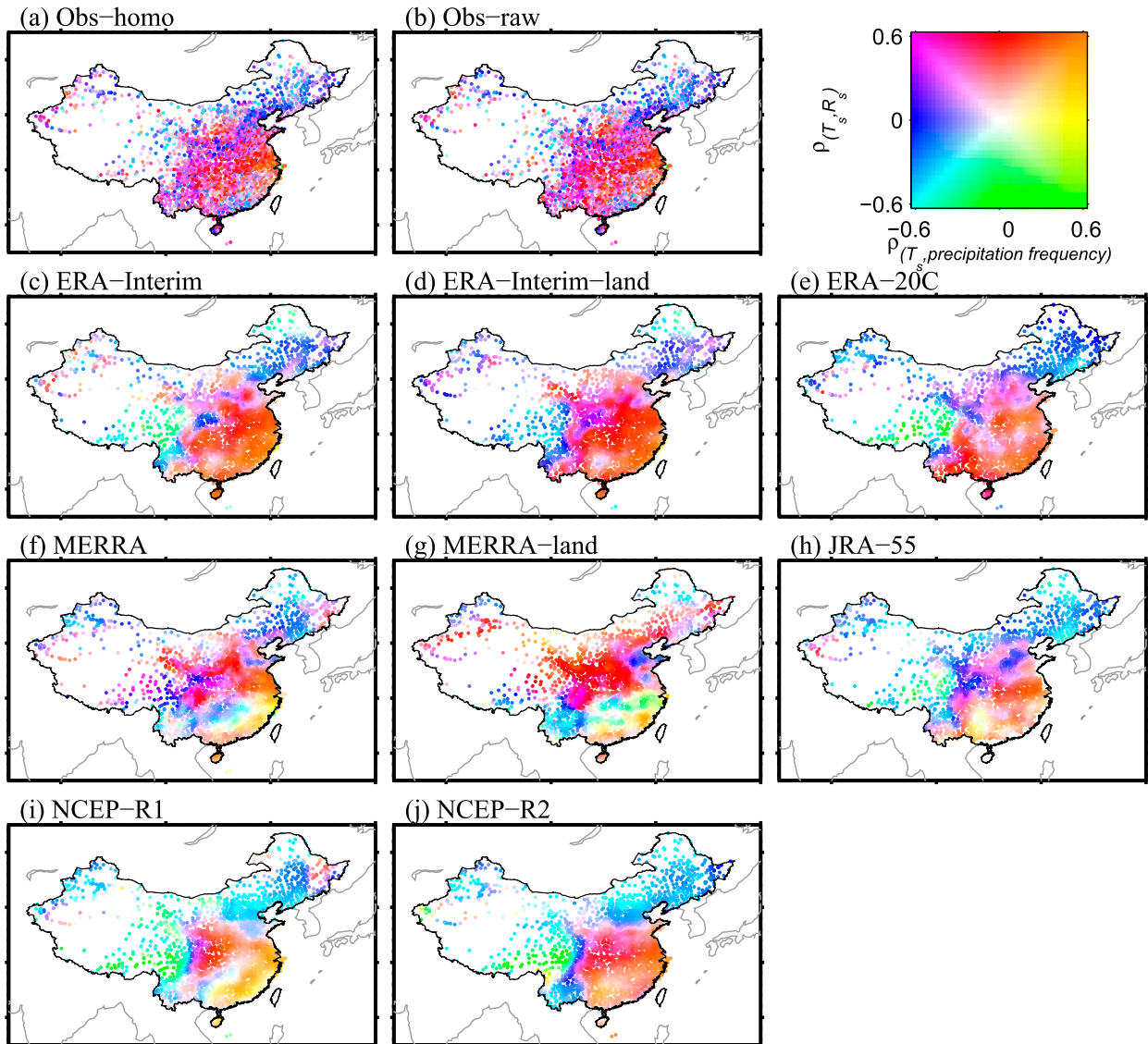


FIG. 4. Composite map of the partial correlation coefficients of T_s against the surface incident solar radiation R_s and precipitation frequency. To avoid a spurious correlation, the detrended time series were used to estimate the partial correlation for 1979 to 2003 from the eight reanalysis products and observations: (a) homogenous observations, (b) raw observations, (c) ERA-Interim, (d) ERA-Interim land, (e) ERA-20C, (f) MERRA, (g) MERRA-land, (h) JRA-55, (i) NCEP-R1, and (j) NCEP-R2. We found that homogenization has only a slight impact on the relationship between T_s and R_s or precipitation frequency.

c. Relationship of land surface temperature to surface incident solar radiation and precipitation frequency

This section will discuss the relationship of T_s against R_s and precipitation frequency. In physics, the R_s heats the surface, largely determining the variability of the T_s at various temporal scales. In turn, the T_s controls the surface-emitted longwave radiation (Wang and Dickinson 2013). Existing studies suggested that precipitation frequency is a better factor in quantifying interannual variability of soil moisture over China than

precipitation amount (Piao et al. 2009; Wu et al. 2012) and then in reflecting vegetation growth and surface characteristics (e.g., surface albedo and roughness). These changes would alter the partitioning of available energy for regulating the change in T_s . Additionally, upper-air raindrops (Fujita 1959; Chen and Wang 1995) or synoptic advection (Trenberth and Shea 2005; Wei et al. 2014) associated with precipitation events also have an inevitable impact on the T_s . We therefore used precipitation frequency instead of precipitation amount in this study. Our following results show that precipitation

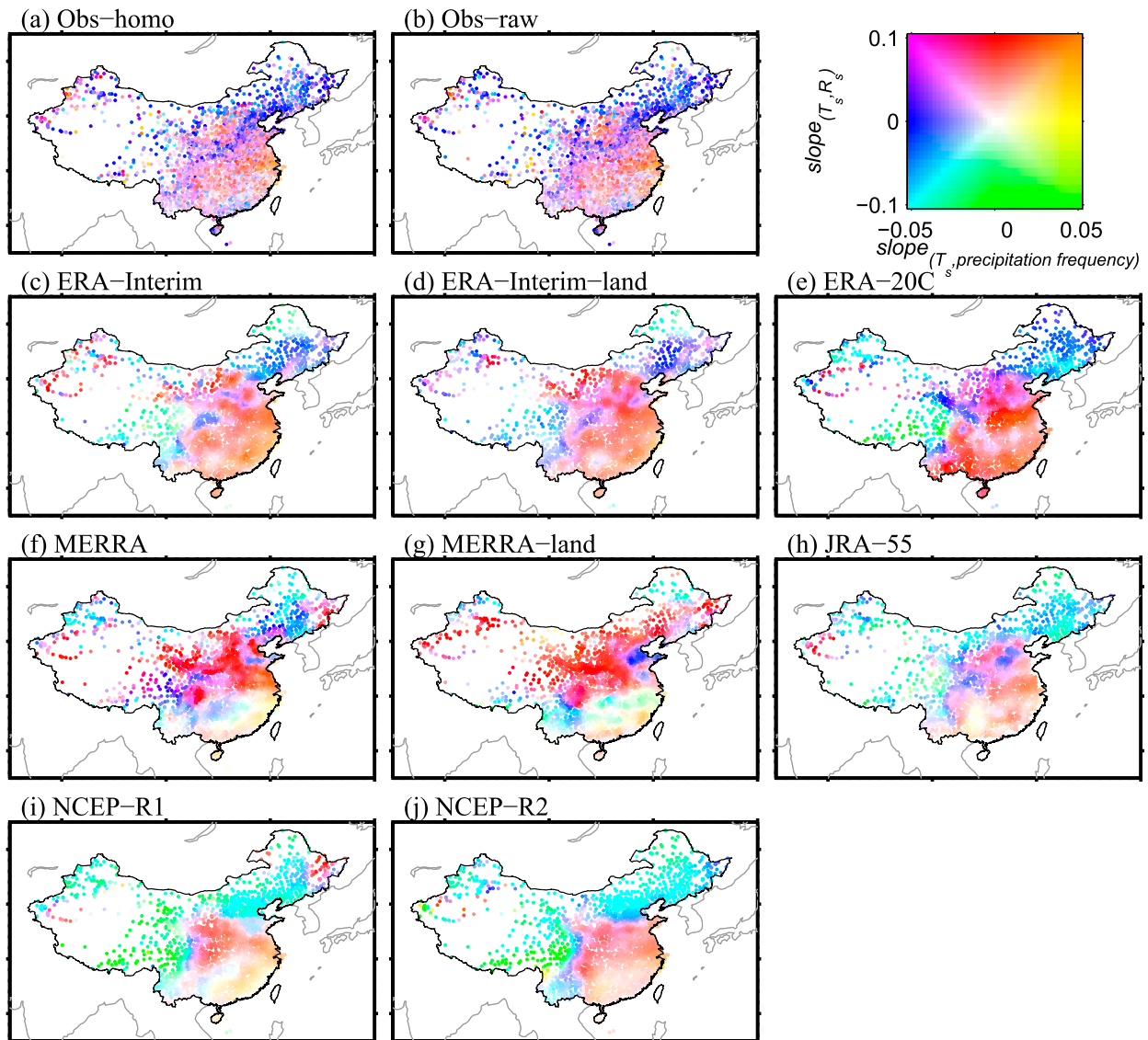


FIG. 5. Composite map of the partial regression coefficients of T_s against the surface incident solar radiation R_s [by controlling for the precipitation frequency [$^{\circ}\text{C} (\text{W m}^{-2})^{-1}$]] and precipitation frequency [by controlling for R_s , [$^{\circ}\text{C} (\text{days})^{-1}$]]. To avoid a spurious correlation relationship, the detrended time series were used to estimate the partial correlation for 1979 to 2003 from the eight reanalysis products: (a) homogenous observations, (b) raw observations, (c) ERA-Interim, (d) ERA-Interim land, (e) ERA-20C, (f) MERRA, (g) MERRA-land, (h) JRA-55, (i) NCEP-R1, and (j) NCEP-R2. We found that homogenization has only a slight impact on the relationship between T_s and R_s or precipitation frequency.

frequency is a good indicator in reflecting precipitation impact on interannual variability and trend of T_s .

Although the seasonal cycle of vegetation coverage impacts the simulated values of T_s , current reanalyses do not allow vegetation to change annually. The T_s is measured over the exposed soil surface that does change with time. Therefore, interannual relationships between R_s (or precipitation frequency) and T_s are expected to be similar in the model and observations. Our results below confirmed this inference. Figures 4 and 5 illustrate the partial relationships between the

annual T_s and R_s anomalies (after controlling for the precipitation frequency) and the precipitation frequency (after controlling for R_s). The homogenization of the data has only a slight impact on the partial relationship of T_s with R_s and the precipitation frequency (Figs. 4 and 5).

In the observations, the interannual variance of T_s is primarily regulated by the precipitation frequency and secondarily by R_s over northwest China, northeast China, and the Tibetan Plateau (Figs. 4, 5, and 6). ERA-Interim, ERA-Interim land, and MERRA can

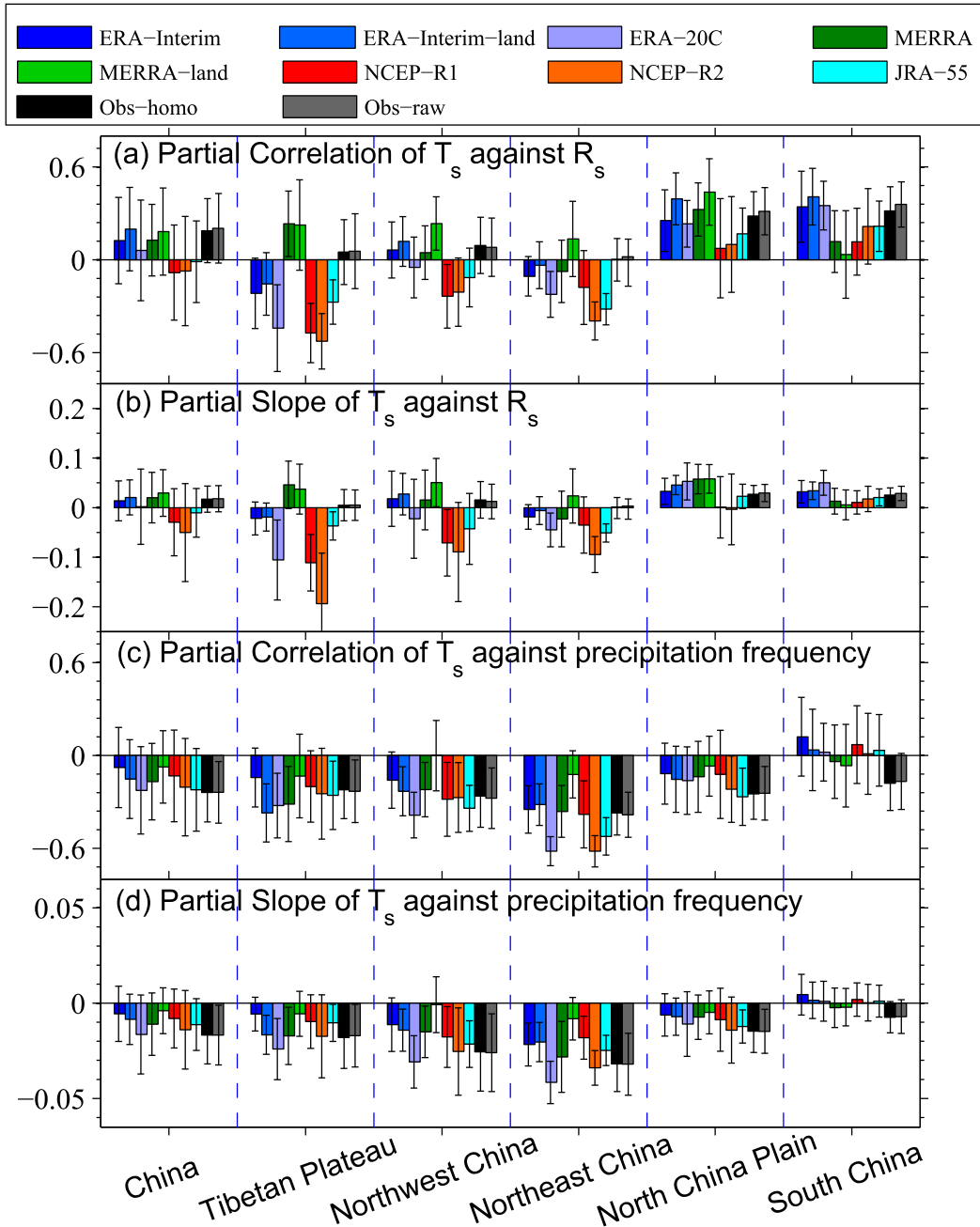


FIG. 6. Regional averages of the partial correlation and regression coefficients of T_s against (a),(b) the surface incident solar radiation R_s (by controlling for the precipitation frequency; units: 1 and $^{\circ}\text{C}/\text{Wm}^{-2}$) and (c),(d) precipitation frequency (by controlling for R_s ; units: 1 and $^{\circ}\text{C}/\text{days}$) over China and its five subregions including the Tibetan Plateau, northwest China, northeast China, the north China plain, and south China. The partial regression was conducted after detrending the time series. The error bars denote the standard deviations of the correlation and regression coefficients.

roughly simulate the observed relationships (Figs. 4, 5, and 6). However, ERA-20C, JRA-55, NCEP-R1, and NCEP-R2 present inaccurately negative partial relationships between T_s and R_s over northwest China and northeast China (Figs. 4, 5, and 6). ERA-20C,

NCEP-R2, and JRA-55 present even stronger negative correlation and regression coefficients between T_s and precipitation frequency than the observations over northeast China (Figs. 4, 5, and 6). MERRA land overestimates the positive correlation and regression

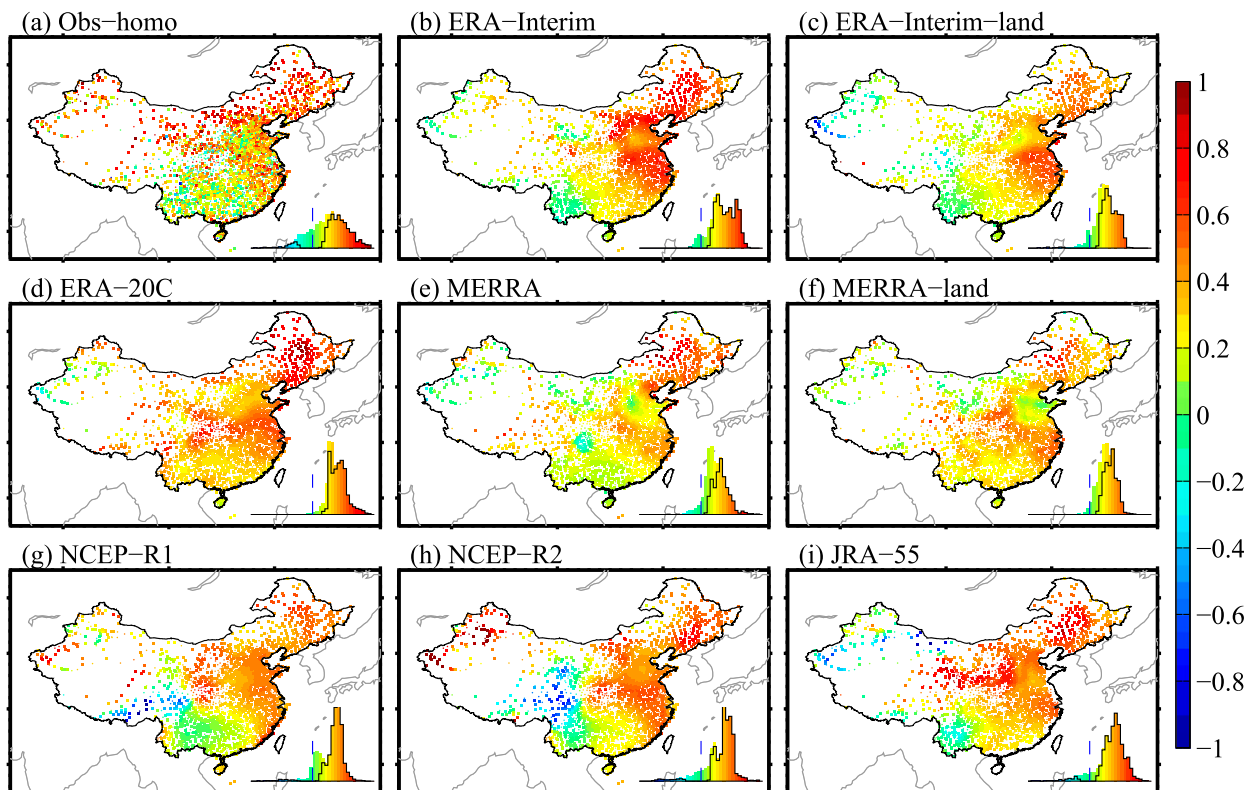


FIG. 7. Land surface temperature T_s ($^{\circ}\text{C decade}^{-1}$) trend maps for 1979 to 2003 from the homogenous observations and the eight reanalysis products: (a) homogenous observations, (b) ERA-Interim, (c) ERA-Interim land, (d) ERA-20C, (e) MERRA, (f) MERRA-land, (g) NCEP-R1, (h) NCEP-R2, and (i) JRA-55. The histogram on the inside right of each panel is the probability distribution function of all trends, and the black stars are integrated from the trends with a significance level of 0.05 (based on a two-tailed Student's t test). The histogram bins correspond to the 40 equal quantities denoted in the color bar.

coefficients between T_s and R_s and underestimates those between T_s and the precipitation frequency over the Tibetan Plateau, northwest China, and northeast China (Figs. 4, 5, and 6). In addition, none of the eight reanalyses can reproduce the observed positive partial relationship between T_s and R_s over the Tibetan

Plateau, especially ERA-20C, NCEP-R1, and NCEP-R2 (Figs. 4, 5, and 6).

According to the observations, the interannual variance of T_s is dominated by R_s and secondarily influenced by the precipitation frequency over the north China plain and south China (Figs. 4, 5, and 6). ERA-Interim, ERA-Interim

TABLE 3. Trends ($^{\circ}\text{C decade}^{-1}$) in land surface temperature T_s from 1979 to 2003 over China and its five subregions from homogeneous observations (Obs-homo), raw observations (Obs-raw), ERA-Interim, ERA-Interim land, ERA-20C, MERRA, MERRA land, NCEP-R1, NCEP-R2, and JRA-55. The time span of MERRA land starts in 1982 because of false input forcings in 1980 and 1981. The bold font indicates a two-tailed Student's t test with a significance level of 0.05.

	China	Tibetan Plateau	Northwest China	Northeast China	North China plain	South China
Obs-homo	0.34	0.32	0.53	0.57	0.29	0.17
Obs-raw	0.42	0.39	0.56	0.61	0.44	0.27
ERA-Interim	0.35	0.24	0.25	0.58	0.48	0.27
ERA-Interim land	0.25	0.11	0.06	0.43	0.35	0.24
ERA-20C	0.42	0.39	0.28	0.67	0.44	0.37
MERRA	0.28	0.32	0.12	0.55	0.29	0.20
MERRA land	0.30	0.32	0.15	0.40	0.30	0.32
NCEP-R1	0.29	-0.09	0.37	0.47	0.46	0.22
NCEP-R2	0.30	-0.26	0.54	0.48	0.43	0.24
JRA-55	0.33	0.38	0.06	0.57	0.52	0.25

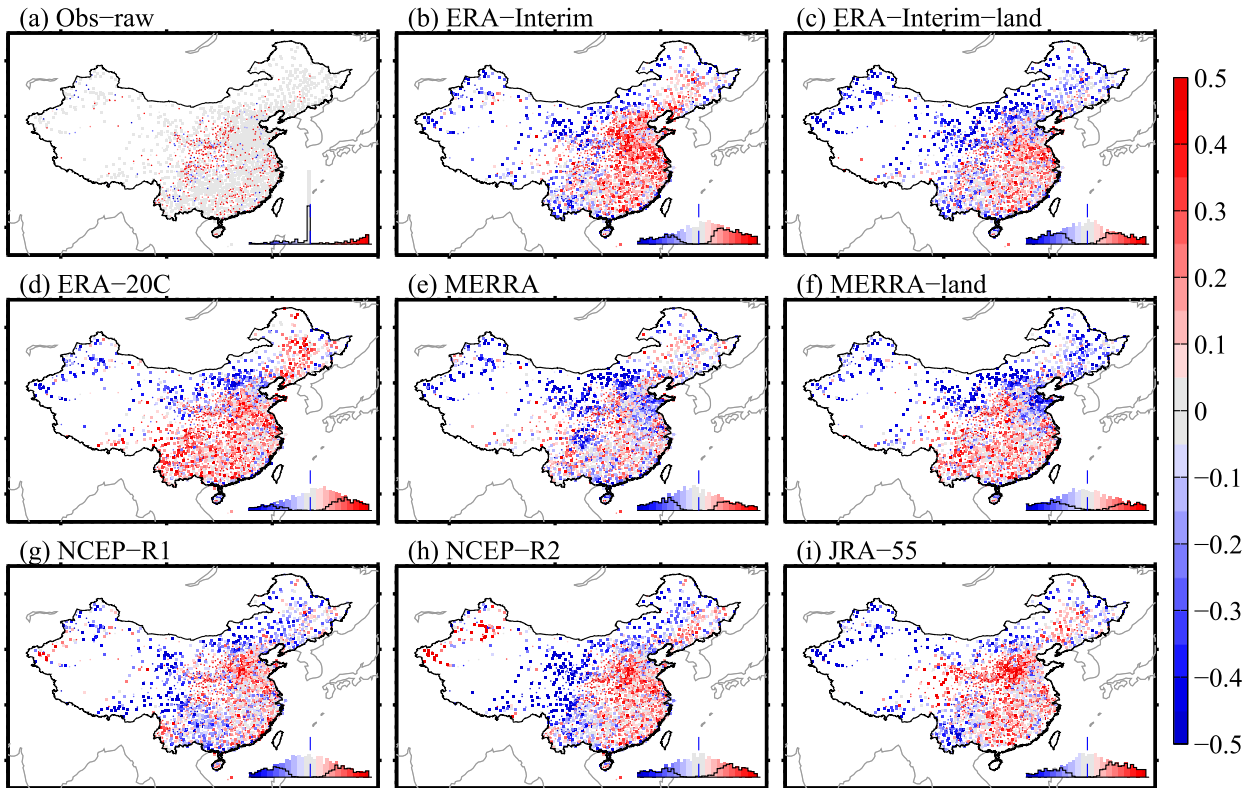


FIG. 8. As in Fig. 7, but for trend differences in the land surface temperature T_s ($^{\circ}\text{C decade}^{-1}$).

land, ERA-20C, and JRA-55 rationally capture the observed relationships over the north China plain and south China (Figs. 4, 5, and 6). MERRA and MERRA land can represent the observed relationships over the North China Plain, and NCEP-R2 can represent the observed relationships over south China (Figs. 4, 5, and 6). However, MERRA, MERRA land, and NCEP-R1 exhibit smaller correlation and regression coefficients between T_s and R_s over south China than those from the observations (Figs. 4, 5, and 6). The same situation occurs over the north China plain for NCEP-R1 and NCEP-R2 (Figs. 4, 5, and 6).

Overall, the observations show that the correlation and regression coefficients between T_s and R_s over humid regions (i.e., the north China plain and south China) are larger than those over arid and semiarid regions (i.e., northwest China, northeast China, and Tibetan Plateau), although the correlation and regression coefficients between T_s and the precipitation frequency over humid regions are smaller than those over arid and semiarid regions (Figs. 4, 5, and 6).

d. Land surface temperature trend

Figure 7 shows a map of the T_s trend from homogenous observations and the eight reanalyses from 1979 to 2003 over China. The T_s exhibits a strong warming trend of $0.34^{\circ}\text{C decade}^{-1}$ (p value from significance t test,

$p < 0.05$) according to the observations and $0.29^{\circ}\text{C decade}^{-1}$ ($p < 0.05$) according to the eight reanalyses over China (Fig. 7 and Table 3).

However, the averaged trends across a large territory may mask regionally different values, reflecting diverse climate change trends and effects. Moreover, there is a stronger observed warming of T_s over northeast China ($0.57^{\circ}\text{C decade}^{-1}$; $p < 0.05$), northwest China ($0.53^{\circ}\text{C decade}^{-1}$; $p < 0.05$), and the Tibetan Plateau ($0.32^{\circ}\text{C decade}^{-1}$; $p < 0.05$) (Fig. 7 and Table 3). Among the eight reanalyses, the increases in R_s and the decreases in precipitation frequency result in the strong warming over northeast China (Fig. 7 and Figs. S2 and S3). However, the eight reanalyses generally underestimate the T_s trend over these regions: $0.40^{\circ}\text{C decade}^{-1}$ – $0.58^{\circ}\text{C decade}^{-1}$ ($p < 0.05$) over northeast China, $0.06^{\circ}\text{C decade}^{-1}$ – $0.37^{\circ}\text{C decade}^{-1}$ over northwest China, and $-0.26^{\circ}\text{C decade}^{-1}$ – $0.39^{\circ}\text{C decade}^{-1}$ over the Tibetan Plateau (Fig. 7 and Table 3). Especially over the Tibetan Plateau, NCEP-R1 and NCEP-R2 present negative trends of -0.09° and $-0.26^{\circ}\text{C decade}^{-1}$, respectively (Fig. 7 and Table 3), which contributed to the failure of NCEP-R1 to simulate surface air temperature trends over the Tibetan Plateau (You et al. 2010; Wang and Zeng 2012).

Furthermore, T_s displays an observed warming of $0.29^{\circ}\text{C decade}^{-1}$ ($p < 0.05$) over the north China plain and $0.17^{\circ}\text{C decade}^{-1}$ ($p < 0.05$) over south China.

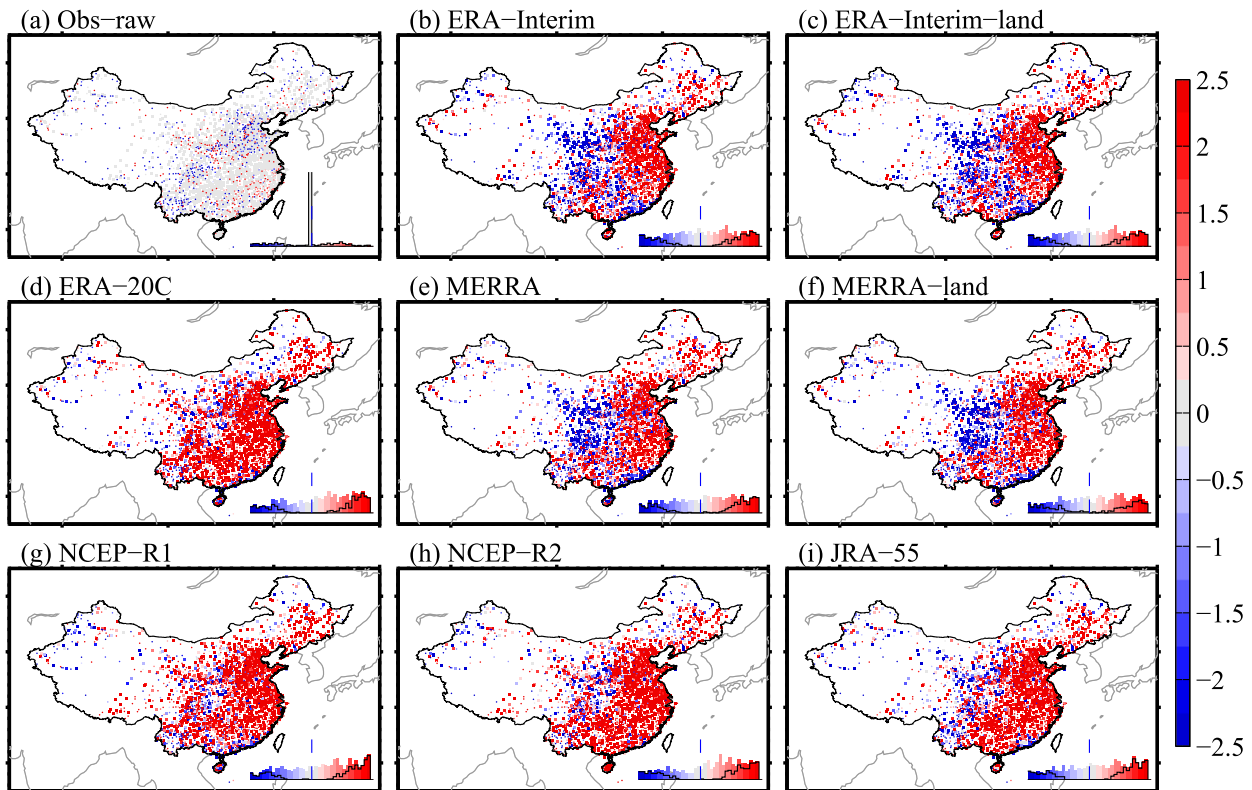


FIG. 9. As in Fig. 7, but for trend differences in the surface incident solar radiation R_s [$(\text{W m}^{-2}) \text{decade}^{-1}$].

Among the eight reanalyses, the decreases in R_s and precipitation frequency result in the relatively weak warming over these regions (Fig. 7 and Figs. S2 and S3). However, the reanalyses overestimate the T_s warming trends over these regions [i.e., $0.29^\circ\text{--}0.52^\circ\text{C decade}^{-1}$ ($p < 0.05$) over the north China plain and $0.20^\circ\text{--}0.37^\circ\text{C decade}^{-1}$ ($p < 0.05$) over south China] because the reanalyses ignored the canceled effect of the increasing aerosol loading (Wang et al. 2015).

We further examined the impact of data homogenization on the T_s trend. The T_s trends derived from the original dataset are always higher than those from the homogenous dataset, especially over the north China plain and south China (Fig. 8a and Table 3). This indicates that the homogenization might adjust the breakpoints in the time series (Wang 2008a) and help to objectively depict the T_s trend, which advances the assessment of the modeled T_s trend in the reanalyses.

e. Contribution of surface incident solar radiation and precipitation frequency to land surface temperature trend biases

Figure 8 shows the trend differences in T_s between the eight reanalyses and the homogenous observation. The

overall pattern in the trend in T_s is underestimated over the Tibetan Plateau and northwest China and overestimated over the north China plain and south China (Fig. 8). Evidently, the R_s trends (Fig. 9) over the north China plain, south China, and northeast China are overestimated by the eight reanalyses, which primarily explains the overestimated T_s trend over the north China plain, south China, and part of northeast China; for example, the spatial pattern correlation between the T_s trend difference and the R_s trend differences is up to 0.77 ($p < 0.05$) over these regions (Figs. 8 and 9). The additional increased R_s trends will heat the land surface and make the T_s trend larger in the reanalyses than in the observations.

The trends in the precipitation frequency are overestimated over northwest China and the Tibetan Plateau and underestimated over northeast China, the north China plain, and south China in the eight reanalyses (Fig. 10). This pattern of differences in precipitation frequency trends substantially explains the underestimated T_s trend over northwest China and the Tibetan Plateau and the overestimated T_s trend over the north China plain, south China, and part of northeast China; for example, the spatial pattern correlation of the T_s trend difference against the R_s trend

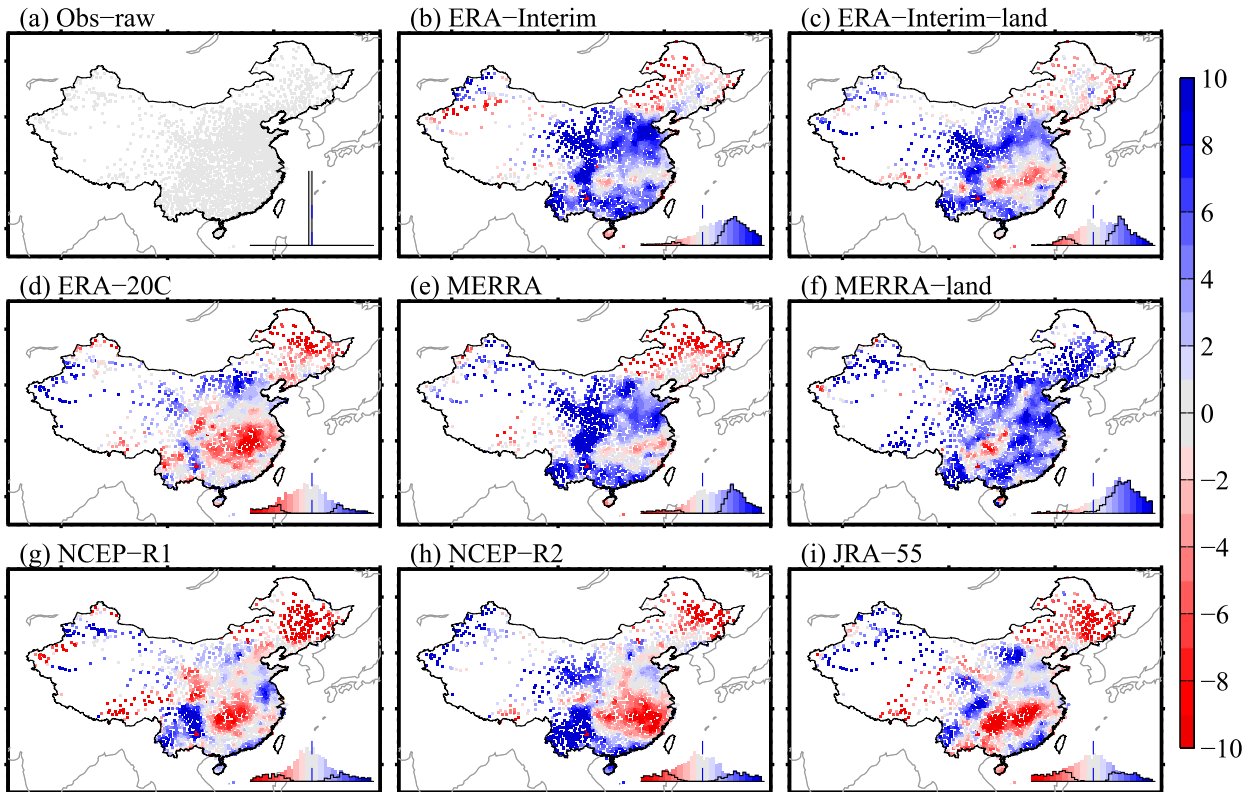


FIG. 10. As in Fig. 7, but for trend difference in the surface precipitation frequency (days decade^{-1}).

differences is up to 0.61 ($p < 0.05$) over China (Figs. 8 and 10). These overestimated trends in the precipitation frequency may contribute to an overestimation of soil surface moisture, allowing, therefore, more available energy for the latent heat flux and in turn leading to surface cooling (Jung et al. 2010; Wang and Dickinson 2012).

By integrating the relationship for the trend biases in T_s with those of R_s and the precipitation frequency over China and its five subregions (Fig. 11), it was found that the underestimated T_s trends in the reanalyses mainly result from the overestimated trends in the precipitation frequency and the underestimated trends in R_s over the Tibetan Plateau and northwest China, whereas the overestimated T_s trends in reanalyses mainly result from the overestimated trends in R_s over the north China plain and south China.

We further quantified the contribution of the trend biases in R_s and the precipitation frequency to those in T_s in the eight reanalyses. Over northwest China and northeast China, the trend biases in R_s (precipitation frequency) can explain 56.3% (40.2%) of the trend biases in T_s in the reanalyses (Fig. 12). The trend biases in T_s are more largely explained by the trend biases in R_s than precipitation frequency because partial sensitivity of T_s to

R_s is more greatly overestimated by reanalyses than to precipitation frequency (Fig. 5). Over the north China plain and south China, the trend biases in R_s (precipitation frequency) can explain 35.1% (26.3%) of the trend biases in T_s in the reanalyses (Fig. 12). Moreover, the sensitivities of the trend biases in T_s to the trend biases in R_s (precipitation frequency) by 0.145 ($^{\circ}\text{C decade}^{-1}$)/[(W m^{-2}) decade^{-1}] [-0.022 ($^{\circ}\text{C decade}^{-1}$)/(days decade^{-1})] over arid and semiarid regions are significantly larger than those over humid regions, that is, 0.034 ($^{\circ}\text{C decade}^{-1}$)/[(W m^{-2}) decade^{-1}] [-0.013 ($^{\circ}\text{C decade}^{-1}$)/(days decade^{-1})] (Fig. 12).

The precipitation frequency might influence R_s through frequent cloud cover (Bony et al. 2015; Norris et al. 2016; Zhou et al. 2016); therefore, we further removed the collinearity of the trend in R_s and the precipitation frequency while quantifying their contribution to the trend biases in T_s . Following this manipulation, the trend differences in R_s (precipitation frequency) can independently explain 45.2% (13.3%) of the trend biases in T_s in the reanalyses over arid and semiarid regions, whereas the trend differences in R_s (precipitation frequency) can independently explain 26.8% (10.8%) of the trend biases in T_s in the reanalyses over humid regions.

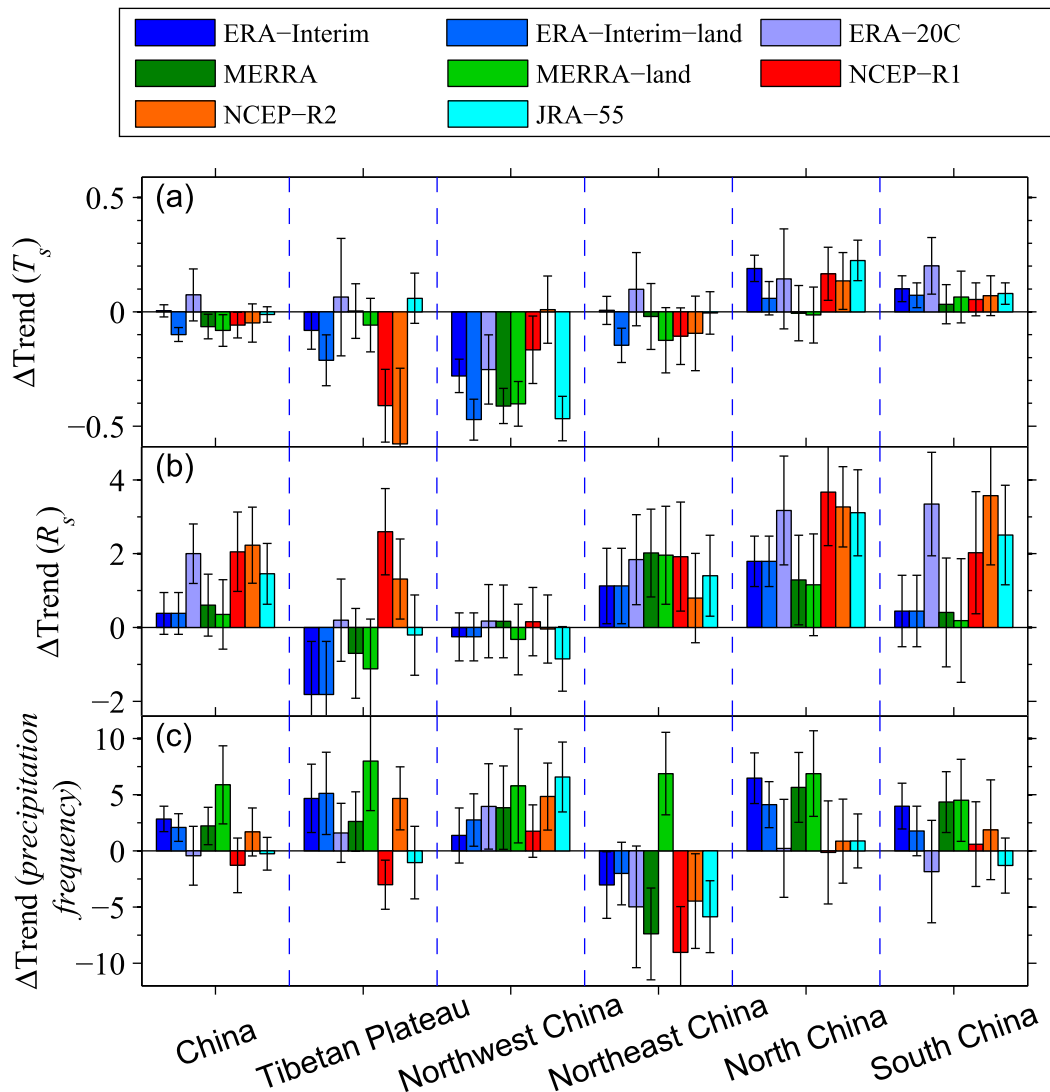


FIG. 11. Trend biases in the (a) land surface temperature T_s ($^{\circ}\text{C decade}^{-1}$), (b) surface incident solar radiation R_s [$(\text{W m}^{-2}) \text{ decade}^{-1}$], and (c) precipitation frequency (days decade^{-1}) for 1979 to 2003 from the eight reanalysis products (ERA-Interim, ERA-Interim land, ERA-20C, MERRA, MERRA-land, JRA-55, NCEP-R1, and NCEP-R2) relative to the homogenous observations over China, the Tibetan Plateau, northwest China, northeast China, the north China plain, and south China. The error bars denote a 95% confidence interval.

In addition, the remaining part of the trend biases in T_s in the reanalyses might be explained by different land surface parameters, including the surface roughness, surface conductivity, friction velocity, turbulent exchange coefficients, vegetation growth, and so forth (Zeng and Dickinson 1998; Veizer et al. 2000; Yang et al. 2006; Zeng et al. 2012; Wang 2014; Zhou and Wang 2016c,e).

4. Conclusions and discussion

The T_s is one of the most important parameters regulating the energy exchange and budget between

Earth's atmosphere and surface, including latent and sensible heat fluxes and longwave radiation, which are closely relevant to climate change. Several previous studies have revealed an underestimation of the diurnal variance in the modeled T_s over sparsely vegetated regions; much effort has been exerted to reduce this bias (Zeng and Dickinson 1998; Yang et al. 2002; Trigo and Viterbo 2003; Chen et al. 2010, 2011; Zeng et al. 2012; Zheng et al. 2012; Wang et al. 2014; Trigo et al. 2015). However, a lack of long-term T_s observations hinders the assessment and improvement of land surface models in reanalyses and hence our understanding of land-atmosphere processes.

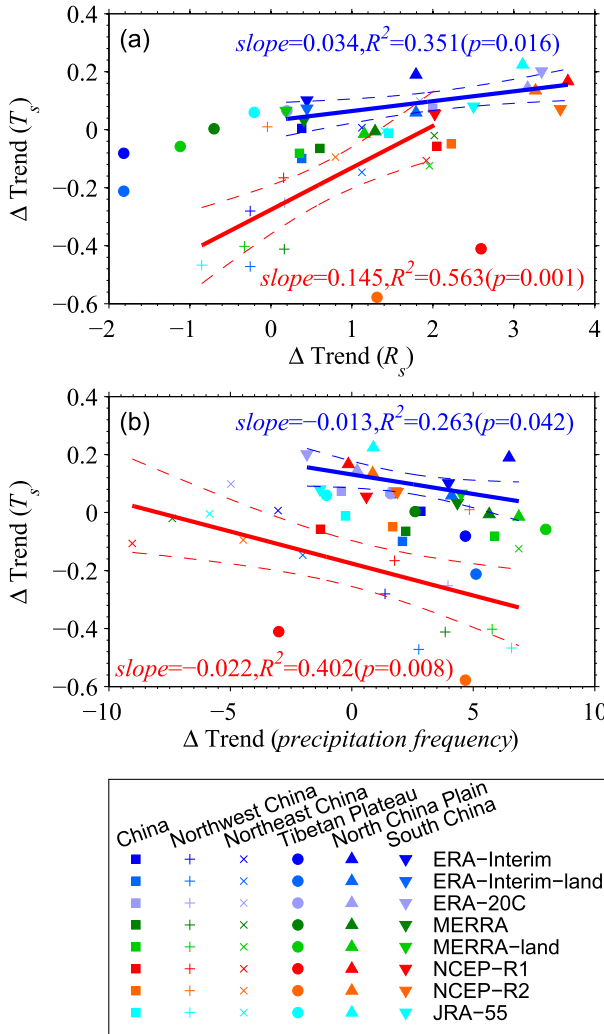


FIG. 12. Scatterplot of the trend biases in the land surface temperature $\Delta \text{trend}(T_s)$ ($^{\circ}\text{C decade}^{-1}$) against those of the (a) surface incident solar radiation $\Delta \text{trend}(R_s)$ [$(\text{W m}^{-2}) \text{ decade}^{-1}$] and (b) precipitation frequency $\Delta \text{trend}(\text{precipitation frequency})$ (days decade^{-1}) for 1979 to 2003 from the eight reanalysis products: ERA-Interim, ERA-Interim land, ERA-20C, MERRA, MERRA-land, NCEP-R1, NCEP-R2, and JRA-55, relative to the homogenous observations over China, the Tibetan Plateau, northwest China, northeast China, north China plain, and South China. The red (blue) lines with the 95% confidence dashed boundary in (a) and (b) are from the ordinary least squares regression of $\Delta \text{trend}(T_s)$ against $\Delta \text{trend}(R_s)$ and $\Delta \text{trend}(\text{precipitation frequency})$, respectively, over the north China plain and south China (northwest China and northeast China). The corresponding regression slopes and R^2 values are listed.

In this study, using long-term T_s observation from 1979 to 2003 at approximately 2200 stations over China, we first comprehensively examined simulated T_s , including the climatology, interannual variances, long-term trend, and their controlling factors, from eight reanalyzed products. The T_s is underestimated in the

eight reanalyses, and the underestimation is the largest over the Tibetan Plateau (-10.89° to -5.44°C). ERA-Interim land and ERA-20C slightly overestimate T_s over the heart of the north China plain mainly because of less aerosol loading in the reanalyses. In regard to the absolute value of T_s , ERA-Interim has the best simulation capacity, whereas ERA-20C, NCEP-R1, and NCEP-R2 give the worst performance.

The reanalyses are skillful in simulating the interannual variance of the T_s anomaly ($r = 0.95$ and $\text{RMSE} = 0.1^{\circ}\text{C}$) over China except over the Tibetan Plateau. ERA-Interim and MERRA land perform better in this aspect than ERA-Interim and MERRA. The interannual variance of T_s is dominated by R_s (having large partial correlation and regression coefficients) and secondarily influenced by the precipitation frequency over the north China plain and south China, whereas it is primarily regulated by the precipitation frequency (having large partial correlation and regression coefficients) and secondarily by R_s over northwest China, northeast China, and the Tibetan Plateau. The interannual domination of T_s is well captured by ERA-Interim, ERA-Interim land, MERRA, and JRA-55.

The T_s observations present a strong warming trend over China ($0.34^{\circ}\text{C decade}^{-1}$). However, the T_s trend is consistently underestimated by the reanalyses over northwest China, the Tibetan Plateau, and part of northeast China and overestimated over the north China plain and south China. We further found that the trend biases in R_s (precipitation frequency) can explain 56.3% (40.2%) of the trend difference in T_s in the reanalyses over northwest China and northeast China and 35.1% (26.3%) of the trend biases in T_s in the reanalyses over north China plain and south China. After removing the collinearity of R_s and the precipitation frequency, the trend biases in R_s (precipitation frequency) can independently explain 45.2% (13.3%) of trend biases in T_s in the reanalyses over arid and semiarid regions and 26.8% (10.8%) of trend biases in T_s in the reanalyses over humid regions. Moreover, the sensitivities of the trend differences in T_s to the trend biases in R_s (precipitation frequency) over arid and semiarid regions are significantly larger than those over humid regions.

Previous studies have mainly focused on the revision of land surface parameterizations, including the surface roughness, surface conductivity, and so forth, to improve the modeled T_s in reanalyses (Zeng and Dickinson 1998; Veizer et al. 2000; Yang et al. 2006; Zeng et al. 2012; Wang 2014). This study shows the importance of R_s and precipitation frequency in determining the variability of T_s , which should be studied in the near future.

Acknowledgments. This study was funded by the National Natural Science Foundation of China (41525018) and the National Basic Research Program of China (2017YFA0603601). The latest precipitation, temperature, and sunshine duration datasets were obtained from the China Meteorological Administration (CMA; <http://data.cma.cn/data>). Considerable gratitude is owed to several reanalysis working teams, including the European Centre for Medium-Range Weather Forecasts (ECMWF) for providing ERA-Interim, ERA-Interim land, and ERA-20C data (<http://www.ecmwf.int/>); the Global Modeling and Assimilation Office (GMAO) at the NASA Goddard Space Flight Center for MERRA and MERRA land data (<http://gmao.gsfc.nasa.gov/>); the NOAA Earth System Research Laboratory (ESRL) for NCEP-R1 and NCEP-R2 data (<http://www.esrl.noaa.gov/>); and the Climate Prediction Division of the Global Environment and Marine Department at the Japan Meteorological Agency for JRA-55 data (<http://jra.kishou.go.jp/>). We thank the Expert Team on Climate Change Detection and Indices (ETCCDI) for the RHtestV4 package (<http://etccdi.pacificclimate.org/software.shtml>).

REFERENCES

- Aarnes, O. J., S. Abdalla, J.-R. Bidlot, and Ø. Breivik, 2015: Marine wind and wave height trends at different ERA-Interim forecast ranges. *J. Climate*, **28**, 819–837, doi:10.1175/JCLI-D-14-00470.1.
- Augustine, J. A., J. J. DeLuisi, and C. N. Long, 2000: SURFRAD—A national surface radiation budget network for atmospheric research. *Bull. Amer. Meteor. Soc.*, **81**, 2341–2357, doi:10.1175/1520-0477(2000)081<2341:SANSRB>2.3.CO;2.
- Baldocchi, D., E. Falge, L. Gu, and R. Olson, 2001: FLUXNET: A new tool to study the temporal and spatial variability of ecosystem-scale carbon dioxide, water vapor, and energy flux densities. *Bull. Amer. Meteor. Soc.*, **82**, 2415–2434, doi:10.1175/1520-0477(2001)082<2415:FANTTS>2.3.CO;2.
- Balsamo, G., A. Beljaars, K. Scipal, P. Viterbo, B. van den Hurk, M. Hirschi, and A. K. Betts, 2009: A revised hydrology for the ECMWF model: Verification from field site to terrestrial water storage and impact in the Integrated Forecast System. *J. Hydrometeorol.*, **10**, 623–643, doi:10.1175/2008JHM1068.1.
- , and Coauthors, 2015: ERA-Interim/Land: A global land surface reanalysis data set. *Hydrol. Earth Syst. Sci.*, **19**, 389–407, doi:10.5194/hess-19-389-2015.
- Beer, C., and Coauthors, 2010: Terrestrial gross carbon dioxide uptake: Global distribution and covariation with climate. *Science*, **329**, 834–838, doi:10.1126/science.1184984.
- Best, M., A. Beljaars, J. Polcher, and P. Viterbo, 2004: A proposed structure for coupling tiled surfaces with the planetary boundary layer. *J. Hydrometeorol.*, **5**, 1271–1278, doi:10.1175/JHM-382.1.
- Bony, S., and Coauthors, 2015: Clouds, circulation and climate sensitivity. *Nat. Geosci.*, **8**, 261–268, doi:10.1038/ngeo2398.
- Carvalho, N., and Coauthors, 2014: Global covariation of carbon turnover times with climate in terrestrial ecosystems. *Nature*, **514**, 213–217, doi:10.1038/nature13731.
- Chen, Y., K. Yang, D. Zhou, J. Qin, and X. Guo, 2010: Improving the Noah land surface model in arid regions with an appropriate parameterization of the thermal roughness length. *J. Hydrometeorol.*, **11**, 995–1006, doi:10.1175/2010JHM1185.1.
- , —, J. He, J. Qin, J. Shi, J. Du, and Q. He, 2011: Improving land surface temperature modeling for dry land of China. *J. Geophys. Res.*, **116**, D20104, doi:10.1029/2011JD015921.
- Chen, Y.-L., and J.-J. Wang, 1995: The effects of precipitation on the surface temperature and airflow over the island of Hawaii. *Mon. Wea. Rev.*, **123**, 681–694, doi:10.1175/1520-0493(1995)123<0681:TEOPOT>2.0.CO;2.
- Dai, A., J. Wang, P. W. Thorne, D. E. Parker, L. Haimberger, and X. L. Wang, 2011: A new approach to homogenize daily radiosonde humidity data. *J. Climate*, **24**, 965–991, doi:10.1175/2010JCLI3816.1.
- Decker, M., M. A. Brunke, Z. Wang, K. Sakaguchi, X. Zeng, and M. G. Bosilovich, 2012: Evaluation of the reanalysis products from GSFC, NCEP, and ECMWF using flux tower observations. *J. Climate*, **25**, 1916–1944, doi:10.1175/JCLI-D-11-00004.1.
- Dee, D. P., E. Källén, A. J. Simmons, and L. Haimberger, 2011a: Comments on “Reanalyses suitable for characterizing long-term trends.” *Bull. Amer. Meteor. Soc.*, **92**, 65–70, doi:10.1175/2010BAMS3070.1.
- , and Coauthors, 2011b: The ERA-Interim reanalysis: Configuration and performance of the data assimilation system. *Quart. J. Roy. Meteor. Soc.*, **137**, 553–597, doi:10.1002/qj.828.
- Dolinar, E. K., X. Dong, and B. Xi, 2016: Evaluation and intercomparison of clouds, precipitation, and radiation budgets in recent reanalyses using satellite-surface observations. *Climate Dyn.*, **46**, 2123–2144, doi:10.1007/s00382-015-2693-z.
- Fujita, T., 1959: Precipitation and cold air production in mesoscale thunderstorm systems. *J. Meteorol.*, **16**, 454–466, doi:10.1175/1520-0469(1959)016<0454:PACAPI>2.0.CO;2.
- Good, E. J., 2016: An in situ-based analysis of the relationship between land surface “skin” and screen-level air temperatures. *J. Geophys. Res. Atmos.*, **121**, 8801–8819, doi:10.1002/2016JD025318.
- Guo, G., X. Zhou, Z. Wu, R. Xiao, and Y. Chen, 2016: Characterizing the impact of urban morphology heterogeneity on land surface temperature in Guangzhou, China. *Environ. Modell. Software*, **84**, 427–439, doi:10.1016/j.envsoft.2016.06.021.
- Jung, M., and Coauthors, 2010: Recent decline in the global land evapotranspiration trend due to limited moisture supply. *Nature*, **467**, 951–954, doi:10.1038/nature09396.
- Kalnay, E., and Coauthors, 1996: The NCEP/NCAR 40-Year Reanalysis Project. *Bull. Amer. Meteor. Soc.*, **77**, 437–471, doi:10.1175/1520-0477(1996)077<0437:TNYRP>2.0.CO;2.
- Kanamitsu, M., W. Ebisuzaki, J. Woollen, S.-K. Yang, J. J. Hnilo, M. Fiorino, and G. L. Potter, 2002: NCEP–DOE AMIP-II Reanalysis (R-2). *Bull. Amer. Meteor. Soc.*, **83**, 1631–1643, doi:10.1175/BAMS-83-11-1631.
- Kobayashi, S., and Coauthors, 2015: The JRA-55 reanalysis: General specifications and basic characteristics. *J. Meteor. Soc. Japan*, **93**, 5–48, doi:10.2151/jmsj.2015-001.
- Ma, L., T. Zhang, Q. Li, O. W. Frauenfeld, and D. Qin, 2008: Evaluation of ERA-40, NCEP-1, and NCEP-2 reanalysis air temperatures with ground-based measurements in China. *J. Geophys. Res.*, **113**, D15115, doi:10.1029/2007JD009549.
- Ma, Y.-M., T.-D. Yao, and J.-M. Wang, 2006: Experimental study of energy and water cycle in Tibetan Plateau: The progress

- introduction on the study of GAME/Tibet and CAMP/Tibet. *Plateau Meteor.*, **25**, 344–351.
- Norris, J. R., R. J. Allen, A. T. Evan, M. D. Zelinka, C. W. O'Dell, and S. A. Klein, 2016: Evidence for climate change in the satellite cloud record. *Nature*, **536**, 72–75, doi:10.1038/nature18273.
- Piao, S. L., L. Yin, X. H. Wang, P. Ciais, S. S. Peng, Z. H. Shen, and S. I. Seneviratne, 2009: Summer soil moisture regulated by precipitation frequency in China. *Environ. Res. Lett.*, **4**, 044012, doi:10.1088/1748-9326/4/4/044012.
- Podobnik, B., and H. E. Stanley, 2008: Detrended cross-correlation analysis: A new method for analyzing two non-stationary time series. *Phys. Rev. Lett.*, **100**, 084102, doi:10.1103/PhysRevLett.100.084102.
- Poli, P., and Coauthors, 2016: ERA-20C: An atmospheric reanalysis of the twentieth century. *J. Climate*, **29**, 4083–4097, doi:10.1175/JCLI-D-15-0556.1.
- Radok, U., and T. J. Brown, 1993: Anomaly correlation and an alternative: Partial correlation. *Mon. Wea. Rev.*, **121**, 1269–1271, doi:10.1175/1520-0493(1993)121<1269:ACAAAP>2.0.CO;2.
- Reichle, R. H., R. D. Koster, G. J. M. De Lannoy, B. A. Forman, Q. Liu, S. P. P. Mahanama, and A. Touré, 2011: Assessment and enhancement of MERRA land surface hydrology estimates. *J. Climate*, **24**, 6322–6338, doi:10.1175/JCLI-D-10-05033.1.
- Rienecker, M. M., and Coauthors, 2011: MERRA: NASA's Modern-Era Retrospective Analysis for Research and Applications. *J. Climate*, **24**, 3624–3648, doi:10.1175/JCLI-D-11-00015.1.
- Ryan, T. P., 2008: *Modern Regression Methods*. 2nd ed. John Wiley and Sons, 672 pp.
- Siswanto, S., G. J. Oldenborgh, G. Schrier, R. Jilderda, and B. Hurk, 2016: Temperature, extreme precipitation, and diurnal rainfall changes in the urbanized Jakarta city during the past 130 years. *Int. J. Climatol.*, **36**, 3207–3225, doi:10.1002/joc.4548.
- Tang, W.-J., K. Yang, J. Qin, C. Cheng, and J. He, 2011: Solar radiation trend across China in recent decades: A revisit with quality-controlled data. *Atmos. Chem. Phys.*, **11**, 393–406, doi:10.5194/acp-11-393-2011.
- Thorne, P., and R. Vose, 2010: Reanalyses suitable for characterizing long-term trends: Are they really achievable? *Bull. Amer. Meteor. Soc.*, **91**, 353–361, doi:10.1175/2009BAMS2858.1.
- Trenberth, K. E., and D. J. Shea, 2005: Relationships between precipitation and surface temperature. *Geophys. Res. Lett.*, **32**, L14703, doi:10.1029/2005GL022760.
- Trigo, I. F., and P. Viterbo, 2003: Clear-sky window channel radiances: A comparison between observations and the ECMWF model. *J. Appl. Meteor.*, **42**, 1463–1479, doi:10.1175/1520-0450(2003)042<1463:CWCRAC>2.0.CO;2.
- , S. Boussetta, P. Viterbo, G. Balsamo, A. Beljaars, and I. Sandu, 2015: Comparison of model land skin temperature with remotely sensed estimates and assessment of surface-atmosphere coupling. *J. Geophys. Res. Atmos.*, **120**, 12 096–12 111, doi:10.1002/2015JD023812.
- Tsidu, G. M., 2012: High-resolution monthly rainfall database for Ethiopia: Homogenization, reconstruction, and gridding. *J. Climate*, **25**, 8422–8443, doi:10.1175/JCLI-D-12-00027.1.
- Veizer, J., Y. Godderis, and L. M. Francois, 2000: Evidence for decoupling of atmospheric CO₂ and global climate during the Phanerozoic eon. *Nature*, **408**, 698–701, doi:10.1038/35047044.
- Viterbo, P., and A. Beljaars, 1995: An improved land surface parameterization scheme in the ECMWF model and its validation. *J. Climate*, **8**, 2716–2748, doi:10.1175/1520-0442(1995)008<2716:AILSPS>2.0.CO;2.
- , —, J. F. Mahfouf, and J. Teixeira, 1999: The representation of soil moisture freezing and its impact on the stable boundary layer. *Quart. J. Roy. Meteor. Soc.*, **125**, 2401–2426, doi:10.1002/qj.49712555904.
- Wang, A., and X. Zeng, 2012: Evaluation of multireanalysis products with in situ observations over the Tibetan Plateau. *J. Geophys. Res.*, **117**, D05102, doi:10.1029/2011JD016553.
- , and —, 2015: Global hourly land surface air temperature datasets: inter-comparison and climate change. *Int. J. Climatol.*, **35**, 3959–3968, doi:10.1002/joc.4257.
- , M. Barlage, X. Zeng, and C. S. Draper, 2014: Comparison of land skin temperature from a land model, remote sensing, and in situ measurement. *J. Geophys. Res. Atmos.*, **119**, 3093–3106, doi:10.1002/2013JD021026.
- Wang, K., 2014: Measurement biases explain discrepancies between the observed and simulated decadal variability of surface incident solar radiation. *Sci. Rep.*, **4**, 6144, doi:10.1038/srep06144.
- , and R. E. Dickinson, 2012: A review of global terrestrial evapotranspiration: Observation, modeling, climatology, and climatic variability. *Rev. Geophys.*, **50**, RG2005, doi:10.1029/2011RG000373.
- , and —, 2013: Global atmospheric downward longwave radiation at the surface from ground-based observations, satellite retrievals, and reanalyses. *Rev. Geophys.*, **51**, 150–185, doi:10.1002/rog.20009.
- , —, M. Wild, and S. Liang, 2012: Atmospheric impacts on climatic variability of surface incident solar radiation. *Atmos. Chem. Phys.*, **12**, 9581–9592, doi:10.5194/acp-12-9581-2012.
- , Q. Ma, Z. J. Li, and J. K. Wang, 2015: Decadal variability of surface incident solar radiation over China: Observations, satellite retrievals, and reanalyses. *J. Geophys. Res. Atmos.*, **120**, 6500–6514, doi:10.1002/2015JD023420.
- Wang, X., and K. Wang, 2016: Homogenized variability of radiosonde-derived atmospheric boundary layer height over the global land surface from 1973 to 2014. *J. Climate*, **29**, 6893–6908, doi:10.1175/JCLI-D-15-0766.1.
- Wang, X. L., 2008a: Penalized maximal F test for detecting undocumented mean shift without trend change. *J. Atmos. Oceanic Technol.*, **25**, 368–384, doi:10.1175/2007JTECHA982.1.
- , 2008b: Accounting for autocorrelation in detecting mean shifts in climate data series using the penalized maximal t or F test. *J. Appl. Meteor. Climatol.*, **47**, 2423–2444, doi:10.1175/2008JAMC1741.1.
- , and Y. Feng, 2013: RHtestsV4 user manual. Environment Canada Atmospheric Science and Technology Directorate Rep., 28 pp. [Available online at <http://etccdi.pacificclimate.org/software.shtml>.]
- , Q. H. Wen, and Y. Wu, 2007: Penalized maximal t test for detecting undocumented mean change in climate data series. *J. Appl. Meteor. Climatol.*, **46**, 916–931, doi:10.1175/JAM2504.1.
- , H. Chen, Y. Wu, Y. Feng, and Q. Pu, 2010: New techniques for the detection and adjustment of shifts in daily precipitation data series. *J. Appl. Meteor. Climatol.*, **49**, 2416–2436, doi:10.1175/2010JAMC2376.1.
- Wei, N., Y. Dai, M. Zhang, L. Zhou, D. Ji, S. Zhu, and L. Wang, 2014: Impact of precipitation-induced sensible heat on the simulation of land-surface air temperature. *J. Adv. Model. Earth Syst.*, **6**, 1311–1320, doi:10.1002/2014MS000322.
- Wen, J., Z. Su, and Y. Ma, 2003: Determination of land surface temperature and soil moisture from Tropical Rainfall Measuring

- Mission/Microwave Imager remote sensing data. *J. Geophys. Res.*, **108**, 4038, doi:10.1029/2002JD002176.
- Weng, Q., D. Lu, and J. Schubring, 2004: Estimation of land surface temperature–vegetation abundance relationship for urban heat island studies. *Remote Sens. Environ.*, **89**, 467–483, doi:10.1016/j.rse.2003.11.005.
- Wold, S., A. Ruhe, H. Wold, and W. J. Dunn, 1984: The collinearity problem in linear regression: The partial least squares (PLS) approach to generalized inverses. *SIAM J. Sci. Stat. Comput.*, **5**, 735–743, doi:10.1137/0905052.
- Wu, C., and Coauthors, 2012: An underestimated role of precipitation frequency in regulating summer soil moisture. *Environ. Res. Lett.*, **7**, 024011, doi:10.1088/1748-9326/7/2/024011.
- Xiao, H., and Q. Weng, 2007: The impact of land use and land cover changes on land surface temperature in a karst area of China. *J. Environ. Manage.*, **85**, 245–257, doi:10.1016/j.jenvman.2006.07.016.
- Yang, K., T. Koike, H. Fujii, K. Tamagawa, and N. Hirose, 2002: Improvement of surface flux parametrizations with a turbulence-related length. *Quart. J. Roy. Meteor. Soc.*, **128**, 2073–2087, doi:10.1256/003590002320603548.
- , —, and B. Ye, 2006: Improving estimation of hourly, daily, and monthly solar radiation by importing global data sets. *Agric. For. Meteorol.*, **137**, 43–55, doi:10.1016/j.agrformet.2006.02.001.
- You, Q., S. Kang, N. Pepin, W.-A. Flügel, Y. Yan, H. Behrawan, and J. Huang, 2010: Relationship between temperature trend magnitude, elevation and mean temperature in the Tibetan Plateau from homogenized surface stations and reanalysis data. *Global Planet. Change*, **71**, 124–133, doi:10.1016/j.gloplacha.2010.01.020.
- Zeng, X., and R. E. Dickinson, 1998: Effect of surface sublayer on surface skin temperature and fluxes. *J. Climate*, **11**, 537–550, doi:10.1175/1520-0442(1998)011<0537:EOSSOS>2.0.CO;2.
- , Z. Wang, and A. Wang, 2012: Surface skin temperature and the interplay between sensible and ground heat fluxes over arid regions. *J. Hydrometeorol.*, **13**, 1359–1370, doi:10.1175/JHM-D-11-0117.1.
- Zheng, W., and Coauthors, 2012: Improvement of daytime land surface skin temperature over arid regions in the NCEP GFS model and its impact on satellite data assimilation. *J. Geophys. Res.*, **117**, D06117, doi:10.1029/2011JD015901.
- Zhou, C., and K. Wang, 2016a: Spatiotemporal divergence of the warming hiatus over land based on different definitions of mean temperature. *Sci. Rep.*, **6**, 31789, doi:10.1038/srep31789.
- , and —, 2016b: Land surface temperature over global deserts: Means, variability and trends. *J. Geophys. Res. Atmos.*, **121**, 14 344–14 357, doi:10.1002/2016JD025410.
- , and —, 2016c: Evaluation of surface fluxes in ERA-Interim using flux tower data. *J. Climate*, **29**, 1573–1582, doi:10.1175/JCLI-D-15-0523.1.
- , and —, 2016d: Coldest temperature extreme monotonically increased and hottest extreme oscillated over Northern Hemisphere land during last 114 years. *Sci. Rep.*, **6**, 25721, doi:10.1038/srep25721.
- , and —, 2016e: Biological and environmental controls on evaporative fractions at AmeriFlux sites. *J. Appl. Meteor. Climatol.*, **55**, 145–161, doi:10.1175/JAMC-D-15-0126.1.
- , and —, 2017: Contrasting daytime and nighttime precipitation variability between observations and eight reanalysis products from 1979 to 2014 in China. *J. Climate*, **30**, 6443–6464, doi:10.1175/JCLI-D-16-0702.1.
- , M. D. Zelinka, and S. A. Klein, 2016: Impact of decadal cloud variations on the Earth's energy budget. *Nat. Geosci.*, **9**, 871–874, doi:10.1038/ngeo2828.
- Zhou, L., R. E. Dickinson, Y. Tian, R. S. Vose, and Y. Dai, 2007: Impact of vegetation removal and soil aridation on diurnal temperature range in a semiarid region: Application to the Sahel. *Proc. Natl. Acad. Sci. USA*, **104**, 17 937–17 942, doi:10.1073/pnas.0700290104.